Title: Cold protection allows local cryotherapy in a clinical-relevant model of traumatic optic neuropathy

Authors: Yikui Zhang[1]*, Mengyun Li[1†], Bo Yu[1†], Shengjian Lu[1†], Lujie Zhang[3†], Senmiao Zhu[1†], Zhonghao Yu[1], Tian Xia[1], Haoliang Huang[2], WenHao Jiang[1], Si Zhang[1], Lanfang Sun[1], Qian Ye[1], Jiaying Sun[1], Hui Zhu[1], Pingping Huang[1], Huifeng Hong[1], Shuaishuai Yu[5], Wenjie Li[3], Danni Ai[3], Jingfan Fan[3], Wentao Li[4], Hong Song[4], Lei Xu[6], Xiwen Chen[7], Jingxing Ou[8, 9], Wei Li[10]*, Jian Yang[3]*, Yang Hu[2]*, Wencan Wu[1]*

Affiliations:

[1] The Eye Hospital, School of Ophthalmology & Optometry, Wenzhou Medical University; Wenzhou 325027, China.

[2] Department of Ophthalmology, Stanford University School of Medicine; Palo Alto, United States.

[3] Beijing Engineering Research Center of Mixed Reality and Advanced Display, School of Optics and Photonics, Beijing Institute of Technology; Beijing 100081, China.

[4] School of Computer Science & Technology, Beijing Institute of Technology; Beijing 100081, China.

[5] School of Laboratory Medicine and Life Sciences, Wenzhou Medical University; Wenzhou 325027, China.

[6] Medical Radiology Department, 2nd Affiliated Hospital, Wenzhou Medical University; Wenzhou 325027, China.

[7] Animal Facility Center, Wenzhou Medical University; Wenzhou 325027, China.

[8] Department of Hepatic Surgery and Liver Transplantation Center of the Third Affiliated Hospital, Guangdong Province Engineering Laboratory for Transplantation Medicine; Guangzhou 510630, China.

[9] Guangdong Key Laboratory of Liver Disease Research, the Third Affiliated Hospital of Sun Yat-sen University, Guangzhou 510630, China

[10] Retinal Neurophysiology Section, National Eye Institute, National Institute of Health, NIH; Bethesda, United States.

* For correspondence: Yikui Zhang: 86-13705770161, zhang.yikui@wmu.edu.cn, Wei Li: 301-496-6669, liwei2@nei.nih.gov, Yang Hu: huyang@stanford.edu, Jian Yang, jyang@bit.edu.cn, Wencan Wu: wuwencan@wmu.edu.cn.

† These authors contributed equally to this work.

Conflict-of-interest statement: The authors have declared that no conflict of interest exists.

Abstract:

Therapeutic hypothermia (TH) is potentially an important therapy for central nervous system (CNS) trauma. However, its clinical application remains controversial, hampered by two major factors: 1) Many of the CNS injury sites, such as the optic nerve (ON), are deeply buried, preventing access for local TH. The alternative is to apply TH systemically, which significantly limits the applicable temperature range. 2) Even with possible access for "local refrigeration", cold-induced cellular damage offsets the benefit of TH. Here we present a clinically translatable model of traumatic optic neuropathy (TON) by applying clinical trans-nasal endoscopic surgery to goats and non-human primates. This model faithfully recapitulates clinical features of TON such as the injury site (pre-chiasmatic ON), the spatiotemporal pattern of neural degeneration, and the accessibility of local treatments with large operating space. We also developed a computer program to simplify the endoscopic procedure and expand this model to other large animal species. Moreover, applying a cold-protective treatment, inspired by our previous hibernation research, enables us to deliver deep hypothermia (4°C) locally to mitigate inflammation and metabolic stress (indicated by the transcriptomic changes after injury) without cold-induced cellular damage, and confers prominent neuroprotection both structurally and functionally. Intriguingly, neither treatment alone was effective, demonstrating that in situ deep hypothermia combined with hibernation-mimicking cold protection constitutes a breakthrough for TH as a therapy for TON and other CNS traumas.

Main Text:

INTRODUCTION

Therapeutic hypothermic (TH) has a long history and was firstly described in the Edwin Smith papyrus over 5000 years ago[1]. Although TH has shown neuroprotection in animal models of central nervous system (CNS) trauma by reducing neuroinflammation and alleviating metabolic demand [2], its clinical application following CNS injury remains controversial. Randomized controlled clinical trials of TH for traumatic brain injury (TBI) failed to show beneficial effect[3-5]. In spinal cord injury (SCI), TH has not been proven to be neuroprotective in randomized controlled clinical trials, and its effect in animal models is inconsistent [2].

At least two major factors hamper the clinical application of TH in CNS trauma. First, many CNS injury sites are located deeply, preventing access for local TH. Instead, TH is applied systemically. But systemic drops in body temperature increase the risk of cardiopulmonary disorders, coagulopathy, and electrolyte disturbances[6], so systemic TH is limited to 34 and 36°C. The limited temperature range of TH may account for its inadequate efficacy. Secondly, even if CNS trauma is accessible for local deep hypothermia, the cold destroys neuronal microtubules andmay counteract the benefit of TH[7]. Our previous study discovered a cold-protective mechanism in hibernators, and found that cold-protective reagents such as protease inhibitors (PI) rescue cold-induced cell damage. If these reagents were applied during local TH, then TH would be a more precise, safe, and effective tool to treat CNS traumas[7].

The optic nerve (ON), which collects axons from retinal ganglion cells (RGCs), is an ideal CNS tissue to study CNS trauma because it is structurally simple.However, its deep location in the orbit and skull base hampers preclinical tests of local treatment for optic neuropathy (**Figure 1A**). Minimally invasive trans-nasal endoscopy is widely used in modern neurosurgeries to

access the distal ON (pre-chiasmatic and chiasmatic ON) in case of tumor or optic canal fracture (**Figure 1B**)[8-11]. The large sphenoid sinus along the distal ON provides sufficient space for local treatment (**Figure 1A-C**). Here we back-translated clinical trans-nasal endoscopy in large animals to safely expose the distal ON, allowing local damage, observation, and modulation. To facilitate clinical translation, we established a *de novo* traumatic optic neuropathy (TON) model in goats and non-human primates by performing pre-chiasmatic ON crush. These models recapitulated clinical features of TON such as the injury site, the time course of progression, and the capability of local treatment *via* trans-nasal endoscopy.

Early transcriptomic changes in the ON and retina were confined to the injury site and enriched in the pathways of inflammation, ischemia, and metabolism, suggesting that local TH could alleviate secondary damage. To serve the twin goals of administrating local deep cooling therapy and preventing cold-induced microtubule instability, we applied both TH and cold-protective reagents. Neither treatment had an effect alone. But when combined, local TH and cold-protective reagents achieved significant structural and functional neuroprotection.

Next, we developed a computer program to detail feasible surgical pathways and to optimize the size of endoscopic tools according to a CT scan of the skull. This program was successful in goats, minipigs, beagles, and rhesus macaques. We trust that this software will help other research groups to replicate our novel TH strategy, and will facilitate preclinical tests for other local TON treatments.

This novel combination of TH and a cold-protection strategy can be readily applied not only in TON patients using the same procedures and devices, but also can potentially revolutionize conventional TH for other CNS trauma such as SCI and TBI. Furthermore, this translatable TON model allows pre-clinical testing of local treatments for axonopathy. This may spark a paradigm

shift in the therapeutic approach for TON, so clinicians can move from less effective strategies (e.g. observation alone, or systemic medication; [12]) towards more targeted and potentially more effective treatment *via* minimally invasive trans-nasal endoscopy.

RESULTS

Goat is an advantageous species for trans-nasal endoscopic access of the chiasmatic and pre-chiasmatic ON

We first looked for animal species suitable for trans-nasal exposure of the chiasmatic and pre-chiasmatic ON. Skull computerized tomography (CT) scan showed that the frontal cortex of the domestic pig and beagle (**Figure 1D**, asterisk) falls between the nasal cavity (**Figure 1D**, number sign) and the pre-chiasmatic ON (**Figure 1D**, blue rectangle), thus blocking surgical access. The narrowest portion of rhesus macaque's sphenoid bone body (**Figure 1D**, red circle) is too narrow (around 2.5 mm in width) to allow a conventional endoscopic microdrill (2.9mm in diameter) to pass through. On the other hand, the size of the goat's sphenoid bone body (13mm in width) is similar to that of the human's sphenoid sinus (20mm in width), and there is no cortex in between the nasal cavity and the pre-chiasmatic ON (**Figure 1D**). Additionally, Saanen goats are readily available, easy to raise and handle, genetically editable[13], and have a genome that is well studied [14-16]. Therefore, we decided to use Saanen goat as our research animal model.

Trans-nasal endoscopic exposure of the pre-chiasmatic ON in goats is feasible and safe

By using clinically available trans-nasal endoscopes (**Supplementary Movie 1**), we exposed the goat's sphenoid bone body (**Figure 1E**), and then removed its anterior cortical bone and inner bone marrow to create an artificial sphenoid sinus. The anterior bony wall of the chiasmatic and

pre-chiasmatic ON laid posteriorly in the sinus (**Figure 1F**). We then exposed the pre-chiasmatic ON by drilling through the anterior bony wall (**Figure 1G, Supplementary Movie 2**).

To evaluate the safety of trans-nasal endoscopic exposure of the pre-chiasmatic ON, we followed the animal for up to 3 months after surgery. The thickness of the ganglion cell complex (GCC, including RGCs' axons, somas and dendrites) in six areas around the optic nerve head was measured by optical coherence tomography (OCT) at different time points (**Figure 1H**). There was no significant change in GCC thickness over 3 months after pre-chiasmatic ON exposure in either the surgical eyes (**Figure 1I**) or the contralateral naïve eyes (**Supplementary Figure 1A**). In line with the OCT results, both the RGC somal densities and axonal densities were unchanged in the surgical eyes compared to the contralateral naïve eyes at 3 months post surgery (3 mps) (**Figure 1J, K**). Consistent with morphological studies, functional readouts (pupillary light reflex (PLR), pattern electroretinogram (PERG), flash visual evoked potential (FVEP) tests) of the surgical eyes were not changed over 3 mps compared with the baseline (**Supplementary Figures 1B, C, D**). Taken together, these results show that endoscopic exposure of the pre-chiasmatic ON is feasible and safe.

Trans-nasal endoscopy-mediated pre-chiasmatic ON crush causes visual loss in goat

Most human TON occur in the pre-chiasmatic ON due to force transmission (**Figure 1B**)[11,17]. To establish a clinically relevant animal model of TON which enables local modulation of the injured pre-chiasmatic ON, we performed pre-chiasmatic ON crush in goat using a trans-nasal endoscopic approach. As illustrated in **Figure 2A**, we first drilled the anterior bony wall to expose the pre-chiasmatic ON, and then manually compressed the pre-chiasmatic ON with the blunt blade of a periosteal elevator until it met the optic canal's posterior bony wall (**Figure 2B, Supplementary Movie 3**).

The visual function of the injured eye was lost after pre-chiasmatic ON crush. Both the direct PLR (dPLR) in the injured eyes and the indirect PLR (iPLR) in the contralateral control eyes disappeared after injury (**Figure 2C**), whereas the dPLR in the contralateral eyes and the iPLR in the injured eyes remained intact (**Supplementary Figure 2A, left panel**). These results suggested that ON function in the injured eyes was lost whereas the contralateral ON was still functional; additionally, the oculo-motor nerves of both eyes were unaffected by pre-chiasmatic ON crush[18]. Consistently, the ratio of the FVEP P1-N1 and P2-N1 amplitudes of the injured eyes to the contralateral eyes decreased significantly compared to the baselines (**Figure 2D**), indicating impairment of the retino-geniculate pathway[19]. Interestingly, the ratio of PERG P1-N1 amplitude of the injured eyes to that of the contralateral eyes remained unchanged at 1 week post injury (1 wpi), then decreased significantly at 1, 2 and 3 months post injury (mpi) compared to the baseline (**Figure 2E**), indicating that RGC function degraded over time[20].

Taken together, the visual deficits (PLR, PERG and FVEP abnormality) presented in the TON model are similar to the clinical manifestations of patients with monocular TON (i.e., Marcus Gunn pupil, loss of visual acuity, and reduction in VEP signals)[21].

Progressive RGC and ON degeneration in goat TON model

The GCC thickness ratio of the injured eyes to contralateral control eyes remained stable at 1 wpi, then decreased progressively over 3 mpi (about 89%, 81%, 74% of the contralateral eyes at 1, 2, 3 mpi, respectively) (**Figure 3A**). The GCC thickness in the contralateral eyes was unchanged after ON crush (**Supplementary Figure 2A, right panel**). Progressive GCC thinning occurred in all six areas around the ON head (**Figure 3A**), indicating that ON crush caused widespread axonal damage with no quadrant being spared. Importantly, the time course of GCC thinning in our model closely resembles that of TON patients[22,23].

There was no significant RGC soma loss at 1 mpi, yet the RBPMS (RNA-binding protein with multiple splicing) immunoreactivity in some RGCs was weak and irregular (**Figure 3B**). At 3 mpi, only 25% of RGCs survived in the injured eyes compared with the contralateral eyes (**Figure 3B**). RGC density in the contralateral eyes remained stable at 1 and 3 mpi (**Supplementary Figure 2B, left panel**). It is worth noticing that our previous study in goat showed that retrobulbar ON crush resulted in more severe RGC loss at 3 mpi (less than 5% survival)[24].

To study the temporal and spatial patterns of axonal degeneration after pre-chiasmatic ON crush, we examined semi-thin cross-sections from four different sites of the ONs (named #1, 2, 3, 4) of both eyes at 1 and 3 mpi (**Figure 3C**). For the contralateral ON, the surviving axonal densities remained statistically the same at 1 and 3 mpi, and there was no significant difference in axonal densities among different ON sites (**Supplementary Figure 2B, right panel**). For the injured eyes, there were few surviving axons at distal regions (#3, #4) at 1 and 3 mpi. In contrast, axonal densities of the proximal ON segments (#1, #2) of the injured eyes were almost intact at 1 mpi and then decreased dramatically at 3 mpi (**Figure 3C**), indicating progressive retrograde axonal degeneration, which was also observed in rodent models of distal ON injury[25].

Taken together, these morphological studies demonstrate progressive retrograde neural degeneration in our TON model, the time course of which is similar to that of clinical TON.

Transcriptomic analysis revealed early changes in ischemia, inflammation, and metabolic pathways at the injured optic nerve

To explore early changes and identify potential therapeutic targets in the injured eye, we sampled from the retina (R), proximal (#1) and pre-chiasmatic (#2) ON segments in both the injured eye and the contralateral eye at 1 day post injury (dpi), and performed RNA-sequencing (**Figure 4A**).

Compared with the contralateral eye, there were few differentially expressed genes (DEGs) in the retina and proximal ON of the injured eye, indicating the transcriptomic status and microenvironment of the retinal and proximal axonal were stable at 1 dpi (**Figure 4B**). In addition, DEGs between the proximal and pre-chiasmatic ON of the contralateral eye were rare, suggesting that the axonal status and microenvironment were consistent between different ON segments (**Figure 4B**). In contrast, there were large amount of DEGs in the injured ON segment (Inj_#3) compared with either the contralateral pre-chiasmatic ON (ctrl_#3) or the ipsilateral proximal ON (Inj_#1). To narrow down the ranges of target genes, we extracted overlapping DEGs between Inj_#3 vs. Ctrl_#3 and Inj_#3 vs. Inj_#1, and found that 91% of the overlapping DEGs were clustered in the pathways of inflammation, ischemia, and metabolism (**Figure 4D, E, Figure S3A**). We further found that most of the DEGs with high connectivity ("hub genes") were also enriched in these pathways (**Figure S4A, B, D**), indicating that targeting these pathways with local treatment could alleviate secondary damage. Gene ontology (GO) analysis of the overlapping DEGs and hub genes is listed in **Figure S3B, S4C**.

Protease inhibitors (PI) rescued cold-induced axonal microtubule damage

Hypothermic therapy can alleviate inflammation and reduce metabolic demand after CNS trauma[2]. However, our previous study showed that the cold destroys neuronal microtubules, and that microtubules can be rescued by cold-protective reagents such as PI[7]. In this study, goat retinal explants cultured at 0°C suffered severe axonal damage compared to those cultured at 37 °C, as shown by beta-3 tubulin-positive axonal length and axonal beads. When we added PI into 0°C medium, this cold-induced axonal degradation was significantly reduced (**Figure 5A-D**).

Trans-nasal local delivery of hypothermia and PI alleviates neural degeneration after pre-chiasmatic ON crush

To prevent axons from degrading during local TH, we applied PI to the injured pre-chiasmatic ON while administering hypothermia locally (**Figures 5E, F, Supplementary Movie 4**). The temperature curves of the cooling water and the cling film over time are shown in **Figure 5G**. The sponge placed at the injury site was filled with goat serum with or without PI.

We found that local combinatory delivery of hypothermia and PI significantly alleviated neural degeneration compared with the no treatment group at 1 mpi in terms of PERG amplitude, GCC thickness and axonal density at the injury site (**Figure 5H-J**). In contrast, local hypothermia or local PI alone failed to show significant neural protection in either PERG signal or GCC thickness (**Figure 5H, I**).

Neither FVEP or PLR were rescued in any treatment group (**Supplementary Figure 5A-C**), since both require an intact ON. In the combinatory treatment group, there were few residual axons at the #4 ON segment (distal to the injury site) (**Supplementary Figure 5D**), indicating Wallerian degeneration was not significantly rescued.

Computer program-aided optimization of trans-nasal endoscopic surgery in multiple large animal species

To simplify the trans-nasal endoscopic surgery and expand the approach to other large animal species, we developed a computer program to generate virtual surgical paths. The flowchart of programming is detailed in **Figure 6A**. Briefly, we input CT scans of the animal's skull into the program to outline the surgical space, the non-surgical space, and the surgical target (**Figure**

6B). Then, we entered the size of the surgical microdrill to generate the surgical corridor (**Figure 6C**).

As shown in **Figure 6D**, there were five degrees of freedom for the surgical corridor when its head met the target (optic canal): rotation around x, y, z axes; spin around the body (major axis); and movement along the neck. We set the step size and ranges of rotation (around x, y, z axes) as 5° and 180°, the step size and ranges of spin as 5° and 360°, the step size and range of movement as 1 mm and 15 mm. Therefore, the total number of theoretical paths were calculated as (180/5)*(180/5)*(180/5)*(360/5)*(15/1) = 50388480. The computer program tried all these theoretical paths to find collision-free surgical corridors within the surgical space. In another words, no pixel of the surgical corridor should be included in the non-surgical space. For example, in **Figure 6E**, the surgical corridor on the right collided with the orbit (non-surgical space, shown in red), so this path was excluded. If there was no feasible surgical pathway with a given size of microdrill, the computer program would reduce the size of the microdrill, and repeat the searching process.

Figure 6F-I shows the virtual surgical paths generated by the computer program to access the pre-chiasmatic ON in goat, beagle, domestic pig and rhesus macaque, respectively. The surgery entry for each species is demonstrated on both the 3D-reconstructed skull (**left panel**) and on the horizontal plane of the CT scan (**middle panel**). The right panels demonstrate the final position of the surgical microdrill when its head meets the target (pre-chiasmatic ON in the optic canal). The step-by-step surgical path plans for goat, beagle, domestic pig and rhesus macaque are presented in **Supplementary Movies 5-8**.

From the computer program, we learn that (1) there are multiple feasible surgical paths in goats (**Figure 6J**), (2) although the frontal cortex in beagles and domestic pigs seems to block access

to the pre-chiasmatic ON (**Figure 1D**), it can be circumvented either inferiorly or laterally (**Figure 6G, H**), and (3) in rhesus macaques, we can access the pre-chiasmatic ON by either circumventing the narrowest portion of the sphenoid bone body (**Figure 6I**) or using a smaller surgical microdrill (2.5 mm in diameter) (**Figure 6K**).

This computer-assisted surgical path planning program can be used to (1) screen suitable animals for trans-nasal endoscopy before surgery, (2) provide a detailed roadmap for endoscopic surgery, and (3) potentially pave the way for robotic surgery to industrialize this novel TON model.

Pre-chiasmatic TON model in rhesus macaques facilitated by computer program-aided optimization

The visual systems of non-human primates (including rhesus macaques) resemble those of humans in terms of macular structure, RGC subtypes, and ON projection pattern[26]. Therefore, we decided to expand our modeling to rhesus macaques. Directly informed by our computer program, we successfully exposed the pre-chiasmatic ON in rhesus macaque *via* trans-nasal endoscopy (**Supplementary Movie 9**), confirmed the target with the surgical navigation system (**Figure S6A**), and performed pre-chiasmatic ON crush (**Figure S6B**).

We observed substantial visual loss and neural degeneration following crush injury. The ratios of PVEP N1-P2 amplitudes and the PERG P1-N1 amplitudes of the injured eyes to the contralateral eyes fell significantly compared with baseline (**Figure S6C, D**). Structurally, GCC thickness in the contralateral eyes did not change over time (**Supplementary Figure 2C**), whereas progressive thinning of GCC was observed in the injured eyes (**Figure S6E**). At 3 mpi, the RGC soma density and the axonal densities at different ON sites of the injured eyes decreased dramatically compared with the contralateral eyes (**Figures S6F, G**).

DISCUSSION

In this study, we developed a novel TH strategy on a *de novo*, translatable, large animal model of CNS axonopathy. Briefly, we back-translated clinical trans-nasal endoscopic surgery into goats and non-human primates to establish a translatable TON model by crushing the pre-chiasmatic ON. This model faithfully resembles the key features of clinical TON, including specific injury site, spatiotemporal pattern of neurodegeneration, and the capability to locally modulate the injured pre-chiasmatic ON. RNA sequencing revealed that early changes were confined to the primary injury site and were enriched in inflammation, ischemia, and metabolism. Local co-delivery of hypothermia with cold-protective reagents showed significant structural and functional neuroprotection, but neither treatment was neuroprotective by itself. To ensure other research groups can faithfully replicate this endoscopy (for TH or for other ON treatments), we made a computer program to optimize surgical paths based on skull CT scans. This study potentially revolutionizes TH for CNS traumas, and provides translatable large animal models for developing local therapeutic strategies for TON and other axonal injuries.

Current treatment for TON

TON causes severe visual loss after head trauma. Currently, no treatment for TON has been proven effective by randomized controlled trials; mostly, mere observation is recommended[21,27]. *In situ* manipulation of the micro-environment of injured CNS axons has proven beneficial in SCI model and peripheral nerve graft transplantation studies[28,29]. However, most of the ON is hard to expose due to its deep location and crowding by neighboring tissues. Drugs delivered systemically or regionally (i.e., intraocularly, intra-orbitally, etc.) can hardly reach the injured distal ON at sufficient and stable concentrations due to the blood brain barrier, diffusion/dilution, and impaired axonal microvasculature[30-32]. Our TON model allows clinically-resembling local

treatment *via* trans-nasal endoscopy with a large operating space. This foundation may trigger a paradigm shift for TON therapies away from mere observation or systemic steroid administration, and towards promising endoscopic treatment.

Hypothermic therapy and cold-protective strategies

Systemic hypothermia may cause coagulopathy, electrolyte disturbances, myocardial ischemia, atrial fibrillation, sepsis, pneumonia, and altered drug metabolism[6]. Instead, we targetted hypothermia to the injured pre-chiasmatic ON to prevent early changes in ischemia, inflammation, and metabolism transcripts (as revealed by RNA-sequencing at 1 dpi).

Although hypothermic therapy was tested as a treatment for CNS trauma for many years, it has not shown neuroprotective effects in randomized controlled trials of TBI or SCI[2,33]. It is unclear why TH was ineffective, but cold-induced neural damage may counteract any therapeutic effects. Our recent work showed that the cold degrades neuronal microtubules, but neurons can be spared with reagents such as PI[7]. In this study, neurons were protected when TH was combined with PI. Neither treatment alone was effective. This novel combinatory strategy can be readily applied to TON patients using established endoscopic procedures, reviving TH as a therapy for TON and other CNS traumas.

Advantages of our TON model compared with other TON models

(1) Clinical translatability: Compared with the conventional retrobulbar ON crush model, our model with pre-chiasmatic ON injury resembles key clinical features of TON such as the specific injury site and the time course of neural degeneration, and allows local trans-nasal treatment using clinical endoscopic procedures and tools. As such, the pre-clinical tests of local treatment for TON succeeded in our model, and can be readily translated to TON patients. Recently, rodent

models have been developed in which ultrasound or impact triggers distal ON injury, but unwanted collateral damage is usually inevitable in these models [34-36]. Besides, clinically translatable, local treatment of injured ONs *via* trans-nasal endoscopy cannot be performed in these rodent models.

Non-human primates including rhesus macaques have human-like visual systems and pathophysiological responses to CNS injury which do not exist in other mammals[26,37,38]. Our work provides goat and non-human primate TON models to meet different experimental needs and budget plans for mechanistic studies or pre-clinical tests of effective treatments.

(2) **Accessibility to the injury site within a large operating space (sphenoid sinus)**: In this study, histological and transcriptomic analyses found that axonal damage was initially confined to the primary injury site. The affected pathways (ischemia, inflammation, and metabolism) offer potential therapeutic targets. In our model, the chiasmatic and pre-chiasmatic ON can be exposed safely under direct visual guidance within the spacious sphenoid sinus, facilitating *in situ* damage, observation, and treatment of the ON with complex devices.

Traditional retrobulbar approach in rodent model allows access only to the most proximal ON within the crowded orbit. Furthermore, exposure of the retrobulbar ON is much harder in human or large animal models, and requires lateral orbitotomy, which causes transient orbital edema and retinal dysfunction[39]. Although access to the distal ON can be achieved by a conventional intra-cranial approach with corticectomy or a recently developed intra-orbital approach by blind injection, these approaches may cause unwanted collateral damage to the important adjacent tissues[40]. In addition, the operating space is restricted in these approaches due to crowding in the cranial cavity or orbital apex.

(3) **Facilitation eye-brain reconnection**: According to our study, the axonal density of the intra-orbital ON segment remained statistically intact 1 mpi; therefore, ON regeneration can start from the pre-chiasmatic ON segment. On the contrary, the traditional retrobulbar ON crush model requires a much longer ON regeneration distance to reconnect with the brain (i.e., the distance is doubled compared with our TON model), making functional regeneration extremely challenging[41]. In addition, our TON model allows local modulation of the microenvironment of the pre-chiasmatic and chiasmatic ON to fuel and guide ON regeneration.

Limitations of this study

One limitation of this study is a small sample size in each therapeutic group. We were aware that an analysis of sample size and power were needed for each comparison. However, due to ethical issue and limitations of housing space and other resources, we only used 3-6 goats/rhesus macaques in each group according to our previous experimental experience. Additionally, we did not repeat TH in rhesus macaques due to budget limitations and ethical concerns. In the near future, we will optimize TH with different onset times of treatment, therapeutic durations, temperature ranges, dosages, and formulae of cold-protective reagents in the goat, and then test the optimized TH strategy in the non-human primate model.

Further application of this model

In the present study, we safely exposed the chiasmatic and pre-chiasmatic ON within the spacious sphenoid sinus. This allows for several promising avenues of research. (1) Access to the ON allows for other ON disorder models, such as optic neuritis or ischemic optic neuropathy, simply by introducing local damage. (2) Optical and electrical diagnostic tools may be placed *in situ*, including confocal endomicroscopy[42] and endoscopic OCT. (3) *In situ* treatments can be tested at the pre-chiasmatic and chiasmatic ON, to prevent axonal degeneration and promote

long-distance axonal regeneration by modulating the micro-environment. These treatments could be partnered with intra-vitreal manipulations to maximize RGC survival and ON regeneration. (4) Our work may potentially be applied in other CNS traumas such as SCI or diffused axonal injury in TBI, as well as early axonal degeneration in Alzheimer's, Parkinson's, and normal aging[43].

MATERIALS AND METHODS

Study Design

This study sought to establish a *de novo*, clinically-relevant, large animal TON framework, and to develop a novel local TH combined with cold protection. Due to ethical issue and limitations of housing space and other resources, we only used 3-6 goats/rhesus macaques in each group according to our previous experimental experience. At least 3 animals were used per test. For *in vivo* tests, histology, and transcriptomic studies, sampling and experimental replicates are detailed in the Methods. For *ex vivo* studies, retinal explants were randomly assigned to three experimental groups (0°C, 0°C with PI, 37°C). For *in vivo* studies, goats from the same company, of the same gender, and of similar ages and weights, were allocated to the groups of injury, hypothermia combined with PI, hypothermia alone, and PI alone without randomization. All the surgeries were performed by one surgeon, and the investigators collecting and analyzing the data were blinded to the grouping. No data outliers were excluded.

Saanen goats and rhesus macaques

Experiments were conducted following the Association for Research in Vision and Ophthalmology (ARVO) Statement for the Use of Animals in Ophthalmic and Vision Research guidelines. All protocols were approved by the Institutional Animal Care and Use Committee in

the Wenzhou Medical University (Wenzhou, China, ID number: wydw2020-0789) and the Joinn Laboratory (Suzhou, China, ID number: P19-S445-PD). 4-7 month-old male Saanen goats weighing 19-22 kg were purchased from the Caimu Livestock Company (Hangzhou, China) and housed in the animal facility of the Wenzhou Medical University. The rhesus macaques aged from 5-7 years weighing 5-7 kg were housed in the animal facility of the Joinn Laboratory. All animals were housed in an air-conditioned room (21 ± 2°C) under a normal light/dark cycle (12/12 hours) with food *ad libitum*. Goats were euthanized with 10% potassium chloride (40 ml, intravenously) after general anesthesia using xylazine (3mg/kg, IM). Rhesus macaques were euthanized by exsanguination after general anesthesia using Zoletil50 (4-8mg/kg, IM, tiletamine/zolazepam).

Trans-nasal endoscopic procedure to expose the pre-chiasmatic ON in goats and rhesus macaques.

Goats were anesthetized with xylazine, and then intubated with a 6.0 mm tracheal tube (Henan Tuoren Medical Device Co., Ltd, China). Anesthesia was maintained with 3% isoflurane in oxygen and air (1:1) at a rate of 2 L/min by using a mechanical ventilator. Then atropine, ceftiofur sodium, gentamicin, dexamethasone, esmolol hydrochloride and hemocoagulase atrox were injected (detailed information of each drug is listed in the “Drug summary”).

After skin preparation with povidone-iodine solution (20 ml, 5%, Zhejiang Apeloa Inc., China), a vertical double-T-shaped incision on the nose was made through the skin and periosteum. Following blunt dissection, the underlying nasal bone was removed to access the nasal cavity. Under trans-nasal endoscopy (Delong, HD380B), the middle turbinate and posterior olfactory nerve filaments were partially removed by an endoscopic microdebrider (Medtronic, 1884004) powered by the Integrated Power Console system (Medtronic, Integrated Power Console ENT

Surgery, 1898001) to expose the ipsilateral anterior wall of the sphenoid bone. To increase surgical operating space, the nasal septum and part of the contralateral olfactory nerve filaments were also resected to fully expose the anterior bony wall of the sphenoid bone (**Figure 1E, left panel**). To access the pre-chiasmatic ON within the sphenoid bone, an endoscopic microdrill (Medtronic, diamond microdrill, 1882969) was employed to drill the overlying cortical bone. The posterior myeloid tissue within the sphenoid bone body (**Figure 1E, right panel**) was aspirated and drilled to create an artificial sphenoid sinus, within which the chiasmatic and pre-chiasmatic ON lay posteriorly (**Figure 1F**). There are two ways to identify the optic canal (part of the pre-chiasmatic ON) in goats during the endoscopic surgery, either by exposing the anterior bony wall of the optic chiasm and then pinpointing the optic canal at the junction of the optic chiasm and the medial orbital wall (**Figure 1G**) or by using a surgical navigation system.

In the sham surgery group, the ON was exposed by drilling through its anterior bony wall (**Figure 1G**). In the ON crush injury group: the ON was crushed by using the blunt blade (3 mm long, 0.5 mm wide) of a periosteal elevator (HBB010, Shanghai Medical Instruments, China) for 5 seconds (**Figure 2A, B**).

Following ON injury, the nasal cavity was irrigated consecutively with povidone-iodine and saline, and the artificial sphenoid sinus was filled with an absorbable gelatin sponge (Xiangen Medical Technology, China). After closure of the nasal periosteum and the skin with 3-0 sutures, anesthesia recovery was conducted.

The trans-nasal endoscopic procedure to expose the optic canal in rhesus macaque was similar to that in goats and used the same surgical equipment. Our self-designed surgical path planning program helped screen for suitable macaques and determine the surgical path based on their pre-surgical cranial CT scans (**Supplementary Movie 9**). The rhesus macaque was anesthetized by

isoflurane (1.5-2%) after induction by Zoletil50 (4-8 mg/kg IM, Virbac, France) in the supine position. The exposed pre-chiasmatic ON was confirmed by a surgical navigation system (NDI Polaris Vicra).

Computer-assisted semi-automated surgical path planning in trans-nasal endoscopic surgery based on CT scans

To facilitate endoscopic exposure and expand this surgical approach to other large animal species, a computer-assisted surgical path planning program was designed based on pre-surgical cranial CT scans. The flowchart of the program is shown in **Figure 6A**. The major steps were as follows:

(1) Virtual reconstruction of surgical space based on cranial CT scans. Cranial CT scans with slice thicknesses of 0.65 mm in goats and 1 mm in beagles and macaques were obtained before surgery (pigs and goats, GE Optina660, General Electric Company, Boston, USA; beagles and macaques, Philip Brilliance iCT, Royal Philips Company, Amsterdam, Holland). The surgical space was manually segmented in the MITK software (MITK, v2018.04.2, detailed code is available in http://mitk.org/wiki/Downloads). The anatomic boundaries of the surgical space were as follows: the nasal and maxillary bone anteriorly, the anterior skull base superiorly, the palate inferiorly, the medial orbital walls laterally, and the posterior wall of the sphenoid body posteriorly (**Figure 6B, in green**). The anterior wall of the left optic canal was marked as the surgical target (**Figure 6B, in yellow**) that needed to be approached by the surgical microdrill.

(2) Virtual reconstruction of the surgical microdrill and the surgical corridor (formed by the movement of the surgical microdrill along its major axis) (**Figure 6C**).

(3) Calculation and optimization of the surgical path. There were five degrees of freedom for the movement of the surgical corridor when its tip met the optic canal (**Figure 6D**). Using a comprehensive search in the program, all possible surgical paths in the three-dimensional virtual space were tested and screened for the most feasible paths in which all the pixels within the surgical corridor were either in the confined surgical space or in air (space outside of the animal's skull) (**Figure 6E**).

(4) Optimization of microdrill size. If no feasible surgical path was identified, the computer automatically decreased the diameter of the surgical microdrill by 0.5 mm, and then repeated steps (1) - (3) to screen for feasible paths.

The code of the computer program is available online (https://github.com/LujieZhang/Preoperative-planning).

Evaluation of microtubule cold-stability in the retinal explants of goats

Goat eyecups were prepared within 15 mins after euthanization with 10% potassium chloride (40 ml, intravenously) in conjunction with general anesthesia using xylazine. Three neighboring retinal pieces, 2 mm in diameter, were taken from the peripheral retina, and randomly assigned to three experimental groups (0°C, 0°C with PI (cold-protective reagent), 37°C) (**Figure 5A**). The retinal explants were pre-treated in hibernate A medium (BrainBits, 2283833, USA) with or without PI (1:500, EMD Millipore Company, 539134, Germany) for 30 minutes at room temperature, then were kept in a 37°C incubator or in a 0°C ice-water mixture for 6 hours. After fixation in 4% PFA for 30 minutes, the retinal explants were immuno-stained against microtubule with beta-3 tubulin (TUBB3) antibody (1:250, from rabbit, Cell Signaling Technology, 5568S, USA), washed in 0.5% Triton in PBS for 5 times, and then were immune-stained with Alexa Fluor 488 conjugated anti-rabbit secondary antibody (1:200, from donkey,

Thermo Fisher Scentific, A-21206, USA). Confocal images were taken under confocal microscopy (Cell Observer SD, ZEISS, Germany) with 63X oil objective lens. Accumulative axonal length of TUBB3-positive optic nerve was analyzed using computer-assisted software ('Simple Neurite Tracer' plugin, ImageJ). Axonal beads along the TUBB3-positive optic nerve were counted manually and bead density was calculated as the number of beads per 100 μm TUBB3-positive optic nerve. For each retinal explant, three regions (108.36 μm x 108.36 μm, 512 x 512 pixels) were imaged, and the accumulative axonal length and axonal bead densities in these three regions were averaged to yield one readout. Retinal pieces with many optic nerve bundles were excluded to facilitate precise quantification. 11 retinal explants from 4 male goats were used in each experimental group. After testing for normality, a repeated measures one-way ANOVA was applied with Dunnett's multiple comparisons test.

Trans-nasal local hypothermic therapy

We developed a trans-nasal local cooling system. Cooling water was pumped into a nasal irrigation tube by a rotary pump (Beijing Zhongshidichuang Technology Development Co., Ltd, China). An irrigation and drainage system consisted of a double-tube cooling device including a pair of concentric silicon tubes. The inner silicon tube (irrigation tube, 3 mm in diameter, Zhejiang Kangkang Medical Equipment Co., Ltd, China) was connected to the pump to receive the cool water. The outer silicon tube (drainage tube, 7 mm in diameter, Taizhou Biling Hardware Products Co., Ltd., China) was covered with cling film (Shanghai Runwen Packaging Materials Co., Ltd., China) to drain the water out of the nasal cavity (**Figure 5E**). A gelfoam sponge (Xiang'en Jiangxi Medical Technology Development Co., Ltd., China) filled with goat serum (Beyotime Institute of Biotechnology, C0265, China) with or without 1:200 diluted PI (EMD Millipore Company, 539134, Germany) was placed between the injured ON and the cling

film (**Figure 5E, F**). To test the effect of hypothermia and PI (cold-protective reagents) on injured ONs, goats were assigned to the following three experimental groups: (1) local hypothermia with PI, (2) local hypothermia without PI, and (3) PI without local hypothermia.

Immediately after the ON crush injury, the sponge was placed at the injury site and then the local cooling tubes were inserted over the gelfoam sponge (**Supplementary Movie 4**). The iced water mixture (0°C as measured by a digital thermometer; ZS-T, Beijing Zhongshidichuang Technology Development Co., Ltd., China) was pumped into the double-tube device to cool the outer surface of the cling film to 4°C (measured by the same digital thermometer). After 2 hours of continuous cooling, the iced water mixture was replaced consecutively with water at 5, 10, 15, and 20°C water for 15 min each to achieve slow rewarming (**Figure 5G**). Then the goat was awakened from general anesthesia. Room temperature was maintained at 23°C.

RNA-sequencing

Fresh samples from the goat's retina, retrobulbar, and pre-chiasmatic ON in injury and contralateral eyes were harvested and frozen in liquid nitrogen within 30 minutes after euthanization at 1 dpi (**Figure 4A**). RNA extraction and sequencing was completed in a bio-company (Biomarker Technologies, China). Total RNA of each sample was extracted following the instruction manual of the TRIzol Reagent (Life Technologies, CA, USA). Agilent 2100 Bioanalyzer (Agilent Technologies, Inc., Santa Clara, CA, USA) was used to test the RNA integrity and concentration. The mRNA was isolated by NEBNext Poly (A) mRNA Magnetic Isolation Module (NEB, E7490), then fragmented into approximately 200 nt RNA inserts. The cDNA library was constructed according to the NEBNext Ultra RNA Library Prep Kit for Illumina (NEB, E7530) and NEBNext Multiplex Oligos for Illumina (NEB, E750), and was sequenced using an Illumina HiSeq™ sequencing platform. The reads were mapped to ARS1

(*Capra hicus*) genome (GenBank assembly accession: GCA_001704415.1) using Tophat2 software. Gene expression levels were estimated using Log2 CPM transformation values on NetworkAnalyst 3.0 website. The raw base call (.bcl) files were converted to demultiplexed FASTQ files with Bcl2fastq v2.19.1 for data analysis. The RNA-sequencing and analysis were repeated in 4 goats. The RNA-seq data has been uploaded online (https://www.ncbi.nlm.nih.gov/geo/query/acc.cgi?&acc=GSE182164).

RNA-seq analysis

Raw reads were assessed using the FastQC toolset (http://www.bioinformatics.babraham.ac.uk/projects/fastqc). The statistics on the raw reads and alignments are shown in sheet 'Mapping Statistics', Data S3. R Subread package was used to quantify gene expression. Adjusted p values from differential expression tests were calculated using the Benjamini-Hochberg procedure for multiple hypothesis testing. Gene ontology (GO) analysis was performed based on hypergeometric test using clusterProfiler package.

To obtain the downstream protein-protein interaction map, the differentially expressed genes were analyzed in the STRING database (https://string-db.org/). Genes that interact more with other genes at the protein level were analyzed in the Cytoscape software (version 3.8.2). The genes with high connectivity were named as hub genes.

Flash visual evoked potential (FVEP)

Visual evoked potential (FVEP) is the cortical potential in response to visual stimulus, reflecting the function of retino-geniculate pathway[19]. FVEP recording in goats has been previously reported in detail[24]. Briefly, following general anesthesia and electrode placement, the animal was adapted to the testing environment for 5 minutes. Then the FVEP was recorded at intensities

of 0.025 and 0.25 cd·s/m^2 consecutively (GT-2008V-III, GOTEC Co., Ltd, China). To reduce variation, we used the FVEP amplitude ratio of the surgical eye to the contralateral eye to quantify the FVEP changes in the surgical eyes.

The pattern visual evoked potential (PVEP) test in rhesus macaques was described previously[24]. The PVEP, which is more reproducible than FVEP in human[19], can be elicited in rhesus macaques according to our previous study[24]. Therefore, we replaced the FVEP test with the PVEP test in rhesus macaques.

Pattern electroretinogram (PERG) recordings

PERG is the retinal electrical signal activated by patterned visual stimuli, the amplitude of which indicates the functional integrity of RGCs[20]. PERG recording in goats and rhesus macaques has been previously reported[24]. Briefly, the goat was anesthetized with xylazine. After electrode placement, PERG signals were elicited by contrast-reversal black-white checkerboards (temporal frequency, 2.4 Hz) at spatial frequencies of 0.1, 0.3, 1.0, 3.0 per degree consecutively (GT-2008V-III, GOTEC Co., Ltd, China). To reduce variation, we report a ratio of the PERG amplitude of the surgical eye to the contralateral eye.

Pupillary light response (PLR) test

The PLR test was used to evaluate the integrity of the ocular afferent (ON) and the efferent (oculomotor nerve) pathways[18]. Direct PLR (dPLR) is the PLR in the ipsilateral eye while indirect PLR (iPLR) occurs in the contralateral eye. This method has been previously described[24]. Briefly, the goat was dark-adapted for 5 minutes after anesthesia with xylazine. Two infrared cameras were positioned at 5 cm from each eye and focused on the pupillary plane to film the PLR. Pupillary constriction was elicited by white light stimulus (230 lx) for two

seconds. The PLR results were scored manually by the same person as follows: Grade 2 (score = 2) = normal PLR; Grade 1 (score = 1) = delayed or weak PLR; Grade 0 (score = 0) = no PLR.

Spectral-domain optical coherence tomography (SD-OCT) imaging

Retinal OCT imaging was used to measure the thickness of the retinal ganglion cell complex including the RNFL, RGC and IPL layers, which represent the RGC axons, somas and dendrites, respectively. This method has been previously described[24]. Briefly, after anesthesia, the OCT images were taken with peripapillary circular scan pattern (Heidelberg Spectralis OCT system, Germany). The thickness of the GCC was measured manually using the Heidelberg software.

Immunohistochemical (IHC) staining of retinal ganglion cells (RGCs)

The IHC staining for RGCs was performed as described in our previous study[24]. Briefly, the eyecup was made and fixed in 4% paraformaldehyde in phosphate-buffered saline (PBS) for 24 h at 4°C. For each retinal quadrant, three circular retinal pieces with a radius of 1 mm were dissected out using a corneal trephine blade (Zhonglindongsheng Medical Instrument, Jiangsu, China) at the central, mid-peripheral and peripheral retina (1/4, 1/2 and 3/4 of the retinal radius away from the ON head, respectively). For each eye, the RGC densities of 12 retinal pieces were averaged to yield one readout. Retinal samples were blocked in 5% goat serum (C0265, Beyotime Institute of Biotechnology, China) in 0.5% PBST overnight, and then incubated in a 1:4000 diluted primary antibody (anti-RBPMS from guinea pig, ProSci, California, custom-made) in 0.5% PBST for 24 h at room temperature. After being washed in PBS, the retinal pieces were incubated in a 1:200 diluted secondary antibody in PBS (Cy3-conjugated, anti-guinea pig from goat, Jackson Immuno Research, West Grove, Pennsylvania) for 12 h at room temperature. The retinal pieces were then washed before being mounted on slides. Confocal images were taken using a Zeiss LSM710 system (Carl Zeiss Meditec, Sartrouville, Germany) under a 20X

objective lens. RBPMS-positive RGCs were counted manually using ImageJ software (NIH, Bethesda, MD, USA).

Quantification of surviving axons within a semi-thin section

Dissection of the ON was completed within 30 mins after euthanization. The ON was cross-sectioned into 1-2 mm-thick discs at the retrobulbar (2 mm behind the eyeball, named as #1), mid-orbital (#2), intra-canalicular (lesion site, #3) and pre-chiasmatic (post-injury site, #4) regions. The ON sections were fixed in 2% glutaraldehyde and 2% PFA in PBS for 24 h at 4°C. After being washed in 0.1 M PB, the samples were incubated in 1% osmium tetroxide in 0.1 M PBS for 1 h and then incubated in 2% uranyl acetate in double distilled water for 1.5 h at 37°C. The samples were then dehydrated through a series of graded ethanol (50% to 100% in H2O) for 10 min at each concentration. The samples were then embedded in 50% EMbed 812/50% propanone for 1 h, followed by a 4:1 ratio of EMbed 812/propanone overnight at 37°C. The next day, the samples were transferred to 100% EMbed 812 for 1 h at 45°C and embedded in a mold filled with 100% EMbed 812 at 45°C for 3 h and then at 65°C for 2 days. Semi-thin sections (2 µm) were cut using an ultramicrotome (LKB-2088, LKB, Bromma, Sweden), stained with 1% para-phenylenediamine (PPD) in methanol: isopropanol (1:1) for 35 min and then rinsed three times with methanol:isopropanol (1:1). Myelin and unhealthy axonal cytoplasm were stained with PPD. More than five separate regions (125.22 µm x 94.26 µm) of each section were imaged at 70X magnification using a Leica DM4B epifluorescence microscope. The surviving axons were semi-automatically counted to obtain the average surviving axonal density for each section. Since the axonal densities amongst different ON sites of the contralateral eyes were statistically the same at 1 and 3 mpi after ON crush (**Supplementary Figure 3C**), we used the axonal density at region #3 to represent the axonal density in the contralateral eye.

Materials & Correspondence

Correspondence and material requests should be addressed to Yikui Zhang, 86-13705770161, zhang.yikui@wmu.edu.cn.

Data and materials availability

Computer program download site:

https://github.com/LujieZhang/Preoperative-planning.

The processed gene expression data in this paper have been deposited into the NCBI GEO database: GSE182164. RNA-seq data download site:

https://www.ncbi.nlm.nih.gov/geo/query/acc.cgi?&acc=GSE182164.

Statistical analyses

All data were analyzed using GraphPad (8.0) software. Normality tests were used to analyze the distributions of all data sets. To compare two groups of data, Student's t-test or nonparametric test was used. To compare multiple groups, a one-way ANOVA (with Dunnett's multiple-comparisons test) or nonparametric Kruskal-Wallis test (with Dunn's multiple-comparisons test) was used. Two-way ANOVA (with multiple comparisons) was used to analyze OCT, PERG, FVEP, PVEP and axonal density data. Asterisks (*) represent statistically significant differences (* $p<0.05$, ** $p<0.01$, *** $p<0.001$, **** $p<0.0001$). Data are presented as mean±s.e.m.

Author contributions:

Conceptualization: YZ, WL, JY, YH, WW

Methodology: YZ, ML, BY, SL, LZ, SZ, HH, QY, JS, WJ, HZ, PH, ZY, TX, WL, DA, JF, HS, YJ, XL, XC, JO, WL, LS, YSS

638 Investigation: YZ, ML, BY, SL, LZ, SZ, HH, QY, JS, WJ, HZ, PH, ZY, TX, WL, DA, JF, HS,

639 YJ, XL, XC, JO, WL, LS

640 Visualization: YZ, ML, SL,

641 Funding acquisition: WW, YZ, JY

642 Project administration: WW, YZ

643 Supervision: YZ, WW

644 Writing – original draft: YZ

645 Writing – review & editing: YZ, JO, WL, YH, WW

Acknowledgments:

We thank Dr. Haohua Qian for critically reading this manuscript. We thank Dr. Michael W. Country for editing this manuscript. We also appreciate Professor Kaihui Nan, Yu Xia, Yuanfei Ji, Mingna Xu, Qiqi Xie, Weijie Liu, Zhaoqi Pan, Xiaohui Jiang, Yao Zhou, Mengting Jin, Haochen Jin for taking part in experimental conduction.

Funding:

National Key R&D Program of China (2016YFC1101200)

National Natural Science Foundation of China (81770926;81800842)

Key R&D Program of Zhejiang Province (2018C03G2090634)

Key R&D Program of Wenzhou Eye Hospital (YNZD1201902)

National Key R&D Program of China (2019YFC0119300)

The sponsor or funding organization had no role in the design or conduct of this research.

Reference

1. Wang, H., Olivero, W., Wang, D. & Lanzino, G. Cold as a therapeutic agent. *Acta Neurochir (Wien)* **148**, 565-570 (2006).
2. Martirosyan, N.L., *et al.* The role of therapeutic hypothermia in the management of acute spinal cord injury. *Clin Neurol Neurosurg* **154**, 79-88 (2017).
3. Clifton, G.L., *et al.* Lack of effect of induction of hypothermia after acute brain injury. *N Engl J Med* **344**, 556-563 (2001).
4. Clifton, G.L., *et al.* Very early hypothermia induction in patients with severe brain injury (the National Acute Brain Injury Study: Hypothermia II): a randomised trial. *The Lancet. Neurology* **10**, 131-139 (2011).
5. Kramer, C., *et al.* Therapeutic hypothermia for severe traumatic brain injury: a critically appraised topic. *The neurologist* **18**, 173-177 (2012).
6. Schubert, A. Side effects of mild hypothermia. *Journal of neurosurgical anesthesiology* **7**, 139-147 (1995).
7. Ou, J., *et al.* iPSCs from a Hibernator Provide a Platform for Studying Cold Adaptation and Its Potential Medical Applications. *Cell* **173**, 851-863.e816 (2018).
8. Chamoun, R. & Couldwell, W.T. Practical and technical aspects of trans-sphenoidal surgery. *J Neurosurg Sci* **55**, 265-275 (2011).
9. Casler, J.D., Doolittle, A.M. & Mair, E.A. Endoscopic surgery of the anterior skull base. *Laryngoscope* **115**, 16-24 (2005).
10. Goudakos, J.K., Markou, K.D. & Georgalas, C. Endoscopic versus microscopic trans-sphenoidal pituitary surgery: a systematic review and meta-analysis. *Clin Otolaryngol* **36**, 212-220 (2011).
11. Yan, W., *et al.* Incidence of optic canal fracture in the traumatic optic neuropathy and its effect on the visual outcome. *The British journal of ophthalmology* **101**, 261-267 (2017).
12. Yu-Wai-Man, P. & Griffiths, P.G. Steroids for traumatic optic neuropathy. *The Cochrane database of systematic reviews*, CD006032-CD006032 (2013).
13. Kalds, P., *et al.* Sheep and Goat Genome Engineering: From Random Transgenesis to the CRISPR Era. *Frontiers in Genetics* **10**(2019).
14. Araújo, A.M.d., *et al.* Genetic diversity between herds of Alpine and Saanen dairy goats and the naturalized Brazilian Moxotó breed. *Genetics and Molecular Biology* **29**, 67-74 (2006).
15. Martin, P., *et al.* Genome-wide association mapping for type and mammary health traits in French dairy goats identifies a pleiotropic region on chromosome 19 in the Saanen breed. *Journal of Dairy Science* **101**, 5214-5226 (2018).
16. Gipson, T.A. Recent advances in breeding and genetics for dairy goats. *Asian-Australas J Anim Sci* **32**, 1275-1283 (2019).
17. Yu-Wai-Man, P. Traumatic optic neuropathy-Clinical features and management issues. *Taiwan journal of ophthalmology* **5**, 3-8 (2015).
18. Kerrison, J.B., *et al.* Quantification of optic nerve axon loss associated with a relative afferent pupillary defect in the monkey. *Arch Ophthalmol* **119**, 1333-1341 (2001).
19. Odom, J.V., *et al.* ISCEV standard for clinical visual evoked potentials (2009 update). *Documenta ophthalmologica. Advances in ophthalmology* **120**, 111-119 (2010).
20. Porciatti, V. Electrophysiological assessment of retinal ganglion cell function. *Exp Eye Res* **141**, 164-170 (2015).
21. Singman, E.L., *et al.* Indirect traumatic optic neuropathy. *Military Medical Research* **3**, 2-2 (2016).
22. Miyahara, T., Kurimoto, Y., Kurokawa, T., Kuroda, T. & Yoshimura, N. Alterations in retinal nerve fiber layer thickness following indirect traumatic optic neuropathy detected by nerve fiber analyzer, GDx-N. *Am J Ophthalmol* **136**, 361-364 (2003).
23. Shi, W., *et al.* Axonal loss and blood flow disturbances in the natural course of indirect traumatic optic neuropathy. *Chin Med J (Engl)* **126**, 1292-1297 (2013).
24. Zhang, Y., *et al.* In vivo evaluation of retinal ganglion cells and optic nerve's integrity in large animals by multi-modality analysis. *Exp Eye Res* **197**, 108117 (2020).
25. Richardson, P.M., Issa, V.M. & Shemie, S. Regeneration and retrograde degeneration of axons in the rat optic nerve. *J Neurocytol* **11**, 949-966 (1982).
26. TM., P. Specializations of the human visual system: the monkey model meets human reality. (ed. Kaas JH, C.C.) 2004:2231-2059 (Boca Raton, FL: CRC Press, 2004).

27. Levin, L.A., Beck, R.W., Joseph, M.P., Seiff, S. & Kraker, R. The treatment of traumatic optic neuropathy: the International Optic Nerve Trauma Study. *Ophthalmology* **106**, 1268-1277 (1999).
28. TH, H. & S, D.G. The translational landscape in spinal cord injury: focus on neuroplasticity and regeneration. *Nature reviews. Neurology* **15**, 732-745 (2019).
29. Aguayo, A.J., *et al.* Degenerative and regenerative responses of injured neurons in the central nervous system of adult mammals. *Philosophical transactions of the Royal Society of London. Series B, Biological sciences* **331**, 337-343 (1991).
30. Upadhyay, R.K. Drug delivery systems, CNS protection, and the blood brain barrier. *Biomed Res Int* **2014**, 869269-869269 (2014).
31. Coles, J.P. Regional ischemia after head injury. *Current opinion in critical care* **10**, 120-125 (2004).
32. Thale, A., Jungmann, K. & Paulsen, F. Morphological studies of the optic canal. *Orbit* **21**, 131-137 (2002).
33. Dietrich, W.D. & Bramlett, H.M. Therapeutic hypothermia and targeted temperature management for traumatic brain injury: Experimental and clinical experience. *Brain Circ* **3**, 186-198 (2017).
34. Evanson, N.K., Guilhaume-Correa, F., Herman, J.P. & Goodman, M.D. Optic tract injury after closed head traumatic brain injury in mice: A model of indirect traumatic optic neuropathy. *PLoS One* **13**, e0197346 (2018).
35. Tao, W., *et al.* A Novel Mouse Model of Traumatic Optic Neuropathy Using External Ultrasound Energy to Achieve Focal, Indirect Optic Nerve Injury. *Sci Rep* **7**, 11779 (2017).
36. Bastakis, G.G., Ktena, N., Karagogeos, D. & Savvaki, M. Models and treatments for traumatic optic neuropathy and demyelinating optic neuritis. *Developmental Neurobiology* **79**, 819-836 (2019).
37. Friedli, L., *et al.* Pronounced species divergence in corticospinal tract reorganization and functional recovery after lateralized spinal cord injury favors primates. *Sci Transl Med* **7**, 302ra134 (2015).
38. Nardone, R., *et al.* Rodent, large animal and non-human primate models of spinal cord injury. *Zoology (Jena)* **123**, 101-114 (2017).
39. Zhang, Y., *et al.* In vivo evaluation of outer retinal function and structure after retrobulbar optic nerve crush by lateral orbitotomy in goats. *Exp Eye Res* **209**, 108652 (2021).
40. Mesentier-Louro, L.A., *et al.* Direct targeting of the mouse optic nerve for therapeutic delivery. *Journal of Neuroscience Methods* **313**, 1-5 (2019).
41. Yang, S.-G., *et al.* Strategies to Promote Long-Distance Optic Nerve Regeneration. *Frontiers in Cellular Neuroscience* **14**(2020).
42. Belykh, E., *et al.* Progress in Confocal Laser Endomicroscopy for Neurosurgery and Technical Nuances for Brain Tumor Imaging With Fluorescein. *Front Oncol* **9**, 554 (2019).
43. Salvadores, N., Sanhueza, M., Manque, P. & Court, F.A. Axonal Degeneration during Aging and Its Functional Role in Neurodegenerative Disorders. *Frontiers in neuroscience* **11**, 451-451 (2017).

748 **Table 1. Drug summary**

Drug	**Function**	**Dosage, delivery**	**Source**
Xylazine	General anesthesia	4mg/kg, intramuscular (IM)	Huamu Animal Health Products, China
Idzoxan	Antagonist of xylazine	1.5mg/kg, IM	Huamu Animal Health Products, China
Propofol	Induction of general anesthesia	5mg/kg, intravenous (IV)	Xian Lipont Enterprise Union Management, China
Isoflurane	General anesthesia	2.5-3.5%, by mechanical ventilator	RWD Life Science, China
Atropine	Reduction of bronchial secretion, cardiac protection	0.05mg/kg, IV	Guangdong Jieyang Longyang Animal Pharmaceutical, China
Esmolol hydrochloride	Reduction of blood pressure	0.2g (2ml) in 48ml saline,	Qilu Pharmaceutical, China

		IV drip infusion	
Hemocoagulase Atrox	Reduction of hemorrhage	1 unit (1 shot), IM	Penglainuokang Pharmaceutical, China
Dexamethasone	Anti-inflammation	5ml (5mg), IV	Kelong Veterinary Medicine, China
Ceftiofur sodium	Prevention of bacterial infection	20mg/kg, IM	Jiangxi Huatu, China
Gentamicin	Prevention of bacterial infection	8mg/kg, IM	Shanxi Ruicheng Kelong Co., Ltd, China

749

750

751 **Figures**

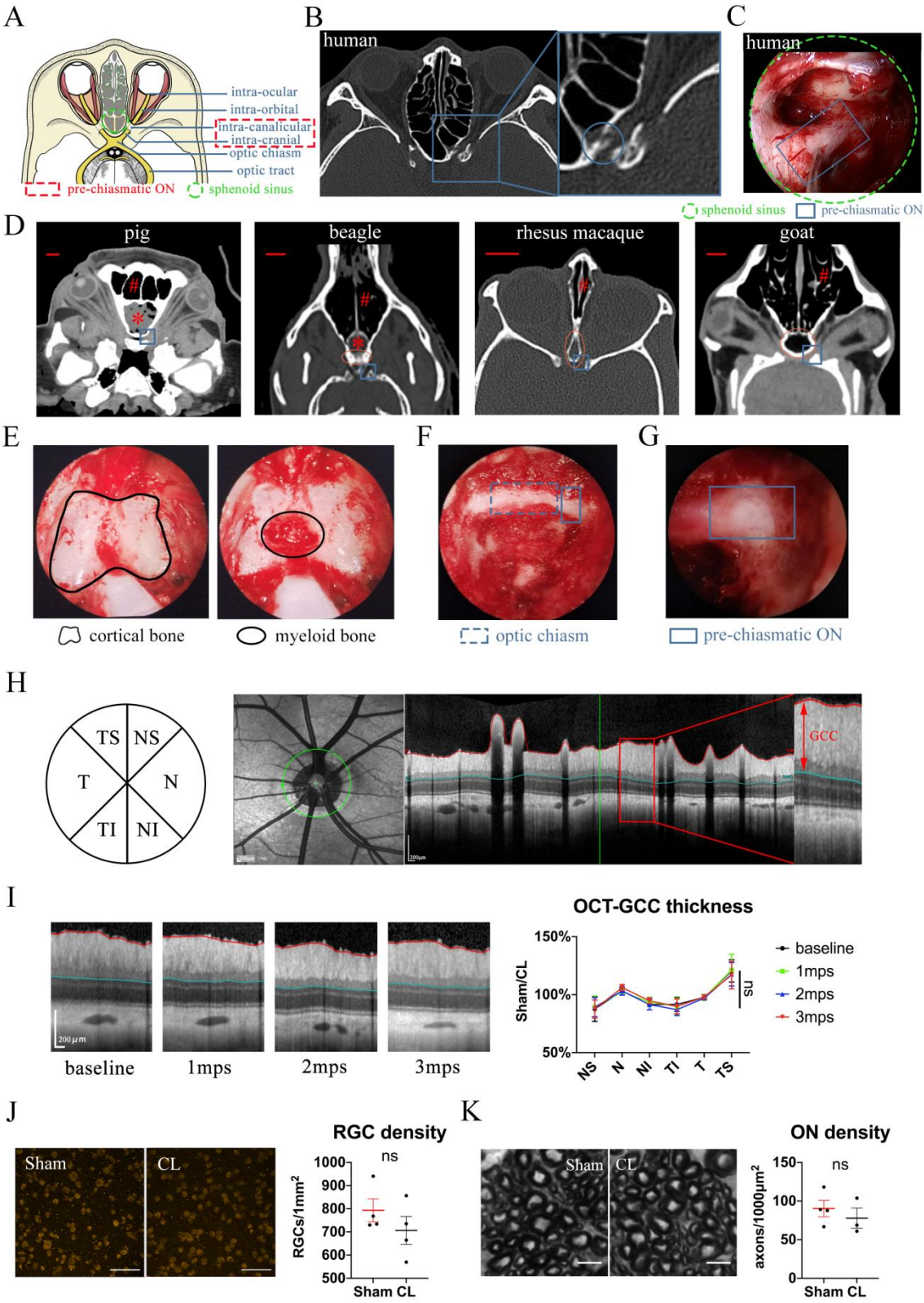

752

753 **Fig. 1. Trans-nasal endoscopic-mediated exposure of pre-chiasmatic ON in goat is feasible**
754 **and safe.** (A) Scheme of anatomic segments of ON and sphenoid sinus (green circle) in
755 human. The pre-chiasmatic ON was shown in the dashed box. (B) CT scan of TON
756 patient with optic canal fracture (blue circle). (C) Endoscopic view of human's pre-
757 chiasmatic ON (blue rectangle) within the large sphenoid sinus (shown in the green
758 circle). (D) Representative skull CT scans of pre-chiasmatic ON (blue rectangle) in pigs,
759 beagles, rhesus macaques and goats. Number sign indicated the nasal cavity. Asterisk
760 indicated the dropping frontal cortex in pigs and beagles. Red circle indicates the
761 sphenoid bone body in beagles, rhesus macaques and goats. Scale bar = 10mm. (E)
762 Endoscopic image of a goat's sphenoid bone body, which is made of cortical bone (left
763 panel) and trabecular bone with myeloid tissue (right panel). (F) Endoscopic image of a
764 goat's chiasmatic ON (blue dashed rectangle) and pre-chiasmatic ON (blue rectangle)
765 with bony wall unremoved. (G) Endoscopic exposure of a goat's pre-chiasmatic ON
766 (blue rectangle) with its anterior bony wall removed. (H) Illustration of GCC thickness
767 measurement by OCT retinal imaging around the optic nerve head in six regions (T:
768 temple, N: nasal; S: superior; I: inferior). (I) Representative OCT images of the eye with
769 its pre-chiasmatic ON exposed (sham surgery eye) (left panel) and quantification of GCC
770 thickness ratio of the sham surgical eyes to the contralateral naïve eyes before and after
771 pre-chiasmatic ON exposure. n=4. Two-way ANOVA with Tukey's multiple comparison
772 (compared with the baseline). (J) Representative immunostaining images of the RBMPS
773 positive RGCs in the retinal flat-mounts (left panel) and quantification of RGCs densities
774 of the sham surgical eyes and the contralateral eyes at 3 months after pre-chiasmatic ON
775 exposure (right panel). n=4. Wilcoxon test. Scale bar = 100 μm. (K) Representative

776 microscopic images of semi-thin cross sections of ON (left panel) and quantification of
777 axonal densities of the sham surgical eyes and the contralateral eyes at 3 months after
778 pre-chiasmatic ON exposure (right panel). n=3-4. Unpaired t-test. Scale bar = 5 μm. Data
779 were presented as mean±s.e.m. ns: p>0.05, not significant. CL: contralateral, mps: month
780 post-surgery (post sham surgery).
781

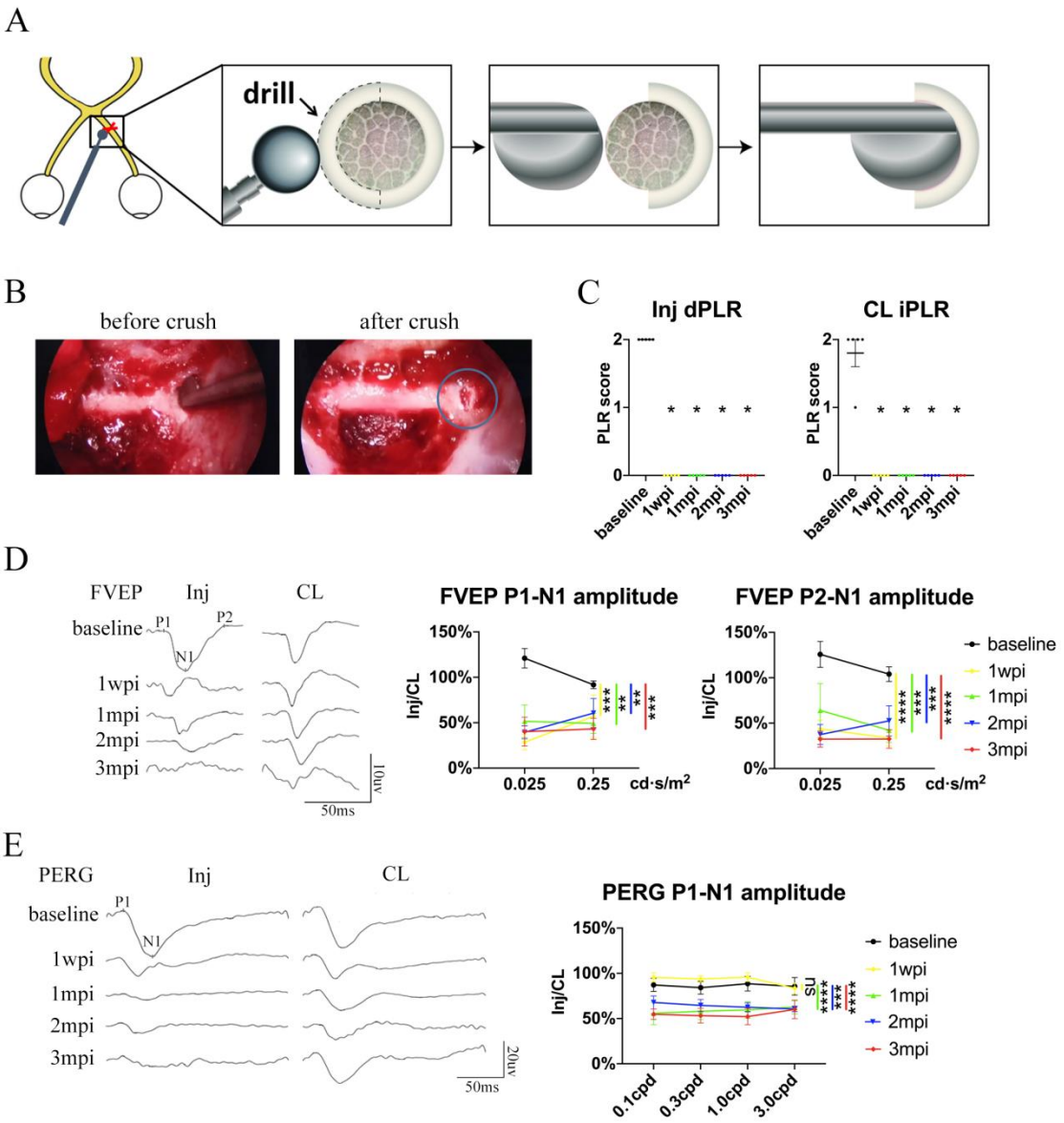

Fig. 2. Trans-nasal endoscopy-mediated pre-chiasmatic ON crush in goat leads to loss of visual function. (A) Schematic illustration of pre-chiasmatic ON exposure and crush injury. (B) Endoscopic views before (left panel) and after pre-chiasmatic ON crush (right panel). Crush site was shown in the blue circle. (C) Loss of direct pupillary light response (dPLR) in the injured eyes (left panel) and indirect PLR (iPLR) in the contralateral eyes (right panel) after crush. Friedman test with Dunn's multiple comparison (compared with

baseline), p=0.0497. (D) Representative FVEP waveforms of the injured eye and the contralateral eye at light intensity of 0.025 cd·s/m^2 (left panel) and quantification of FVEP P1-N1 and P2-N1 amplitudes ratios of the injured eyes to the contralateral eyes (right panel) at different time points before and after pre-chiasmatic ON crush. Two-way ANOVA with Tukey's multiple comparison (compared with the baseline). (E) Representative PERG waveforms of the injured eye and contralateral eye at spatial frequency of 0.1 cpd (left panel) and quantification of PERG P1-N1 amplitude ratios of the injured eyes to the contralateral eyes at spatial frequencies of 0.1, 0.3, 1.0, 3.0 cpd (right panel) before and after pre-chiasmatic ON crush. Two-way ANOVA with Tukey's multiple comparison (compared with the baseline). Data were presented as mean±s.e.m, n=5. ns: not significant, * $p<0.05$, ** $p<0.01$, *** $p<0.001$, **** $p<0.0001$. Inj: injured, CL: contralateral, wpi: week post-injury, mpi: month post-injury.

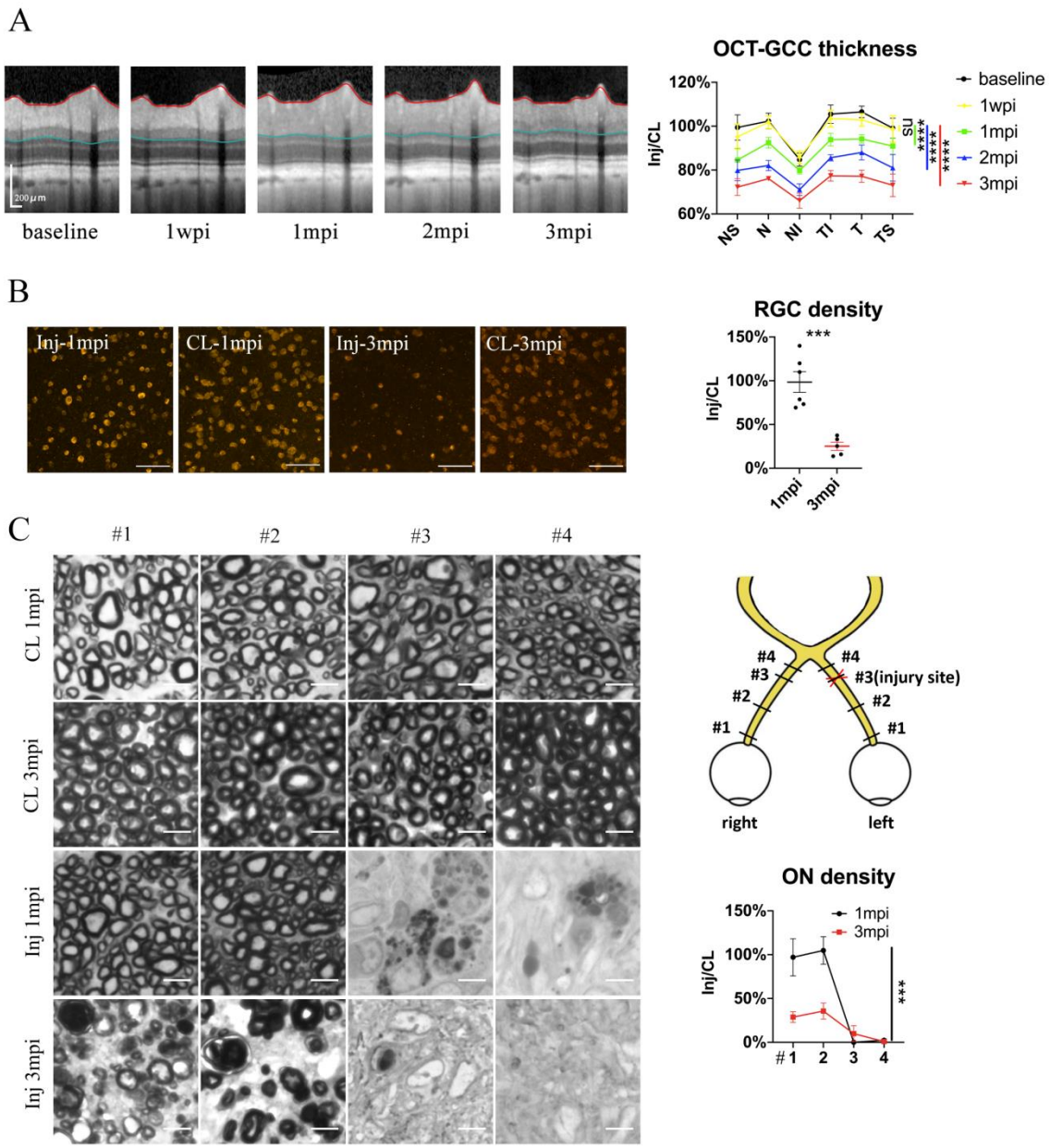

Fig. 3. Spatiotemporal pattern of RGC and ON degeneration in goat TON model. (A) Representative OCT images of the injured eye (left panel) and quantification of GCC thickness ratios of the injured eyes to that of the contralateral eyes at six regions around ON head (right panel) before and after pre-chiasmatic ON crush. n=5. Two-way ANOVA with Tukey's multiple comparison (compared with the baseline). (B) Representative immunostaining images of the RBMPS positive retinal ganglion cells (RGCs) in the

retinal flat-mounts (left panel) and quantification of RGCs densities ratios of the injured eyes to the contralateral eyes at 1, 3 mpi (right panel). n=5-6. Unpaired t-test. Scale bar=100μm. (C) Left panel: representative microscopic images of semi-thin cross sections of ON stained by PPD at different ON segments of the injured eye and its contralateral eye at 1, 3 mpi. Scale bar=5μm. Right upper panel: scheme of sampling sites at different ON segments (#1, 2, 3, 4). Right lower panel: quantification of axonal densities ratios of the injured eyes to the contralateral eyes at different ON segments at 1 and 3 mpi. n=5. Two-way ANOVA. Data were presented as mean±s.e.m. ns: not significant, * $p<0.05$, ** $p<0.01$, *** $p<0.001$, **** $p<0.0001$. Inj: injured, CL: contralateral, wpi: week post-injury, mpi: month post-injury.

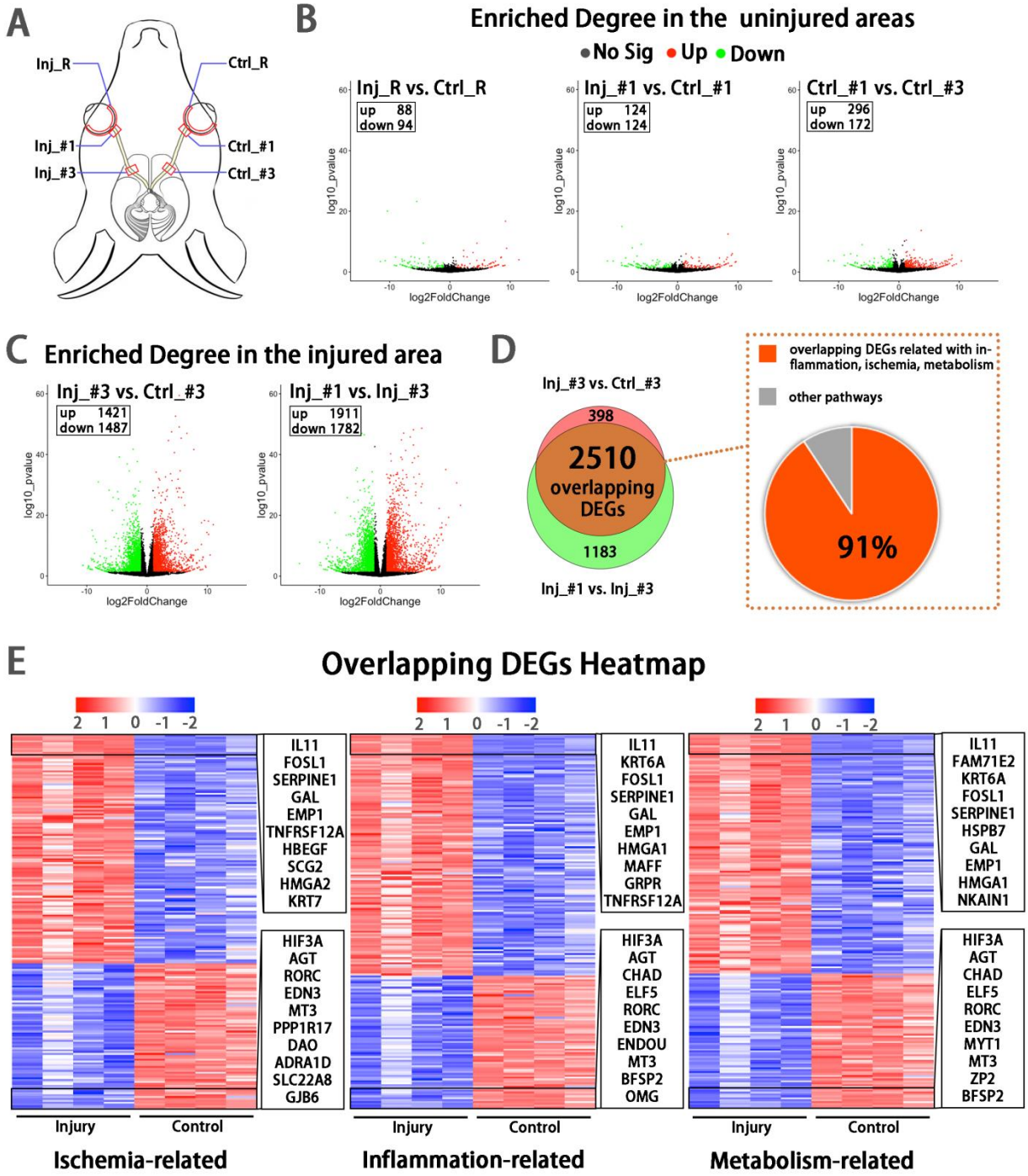

Fig. 4. Early transcriptomic changes are confined to the injury site and mostly enriched in the pathways of ischemia, inflammation and metabolism. (A) Scheme of sampling sites at the retina (R), retrobulbar (#1) and pre-chiasmatic ON (#3) of the injury eye (Inj)

and its contralateral eye (Ctrl). (B, C) Volcano plots showing differential expression genes (DEGs) in the non-injured areas (B) and the injured areas (C). Red dots: significant upregulated genes, green dots: significant downregulated genes, adjusted $p<0.05$. log2FC is 1. (D) Venn diagram indicating the overlapping DEGs between Inj_#3 vs. Ctrl_#3 (ipsilateral-contralateral comparison) and Inj_#3 vs. Inj_#1 (proximal-distal comparison of the ipsilateral eye) (left panel), 91% of which were clustered in the pathways of inflammation, ischemia and metabolism (right panel). (E): Heatmap showing TOP 200 overlapping DEGs related with pathways of ischemia (left panel), inflammation (mid panel) and metabolism (right panel) based on the DEGs of Inj_#3 vs. Ctrl_#3. Ranking was determined by the magnitude of fold change. Upper box shows the top 10 up-regulated genes, and the below one shows the top 10 down-regulated genes.

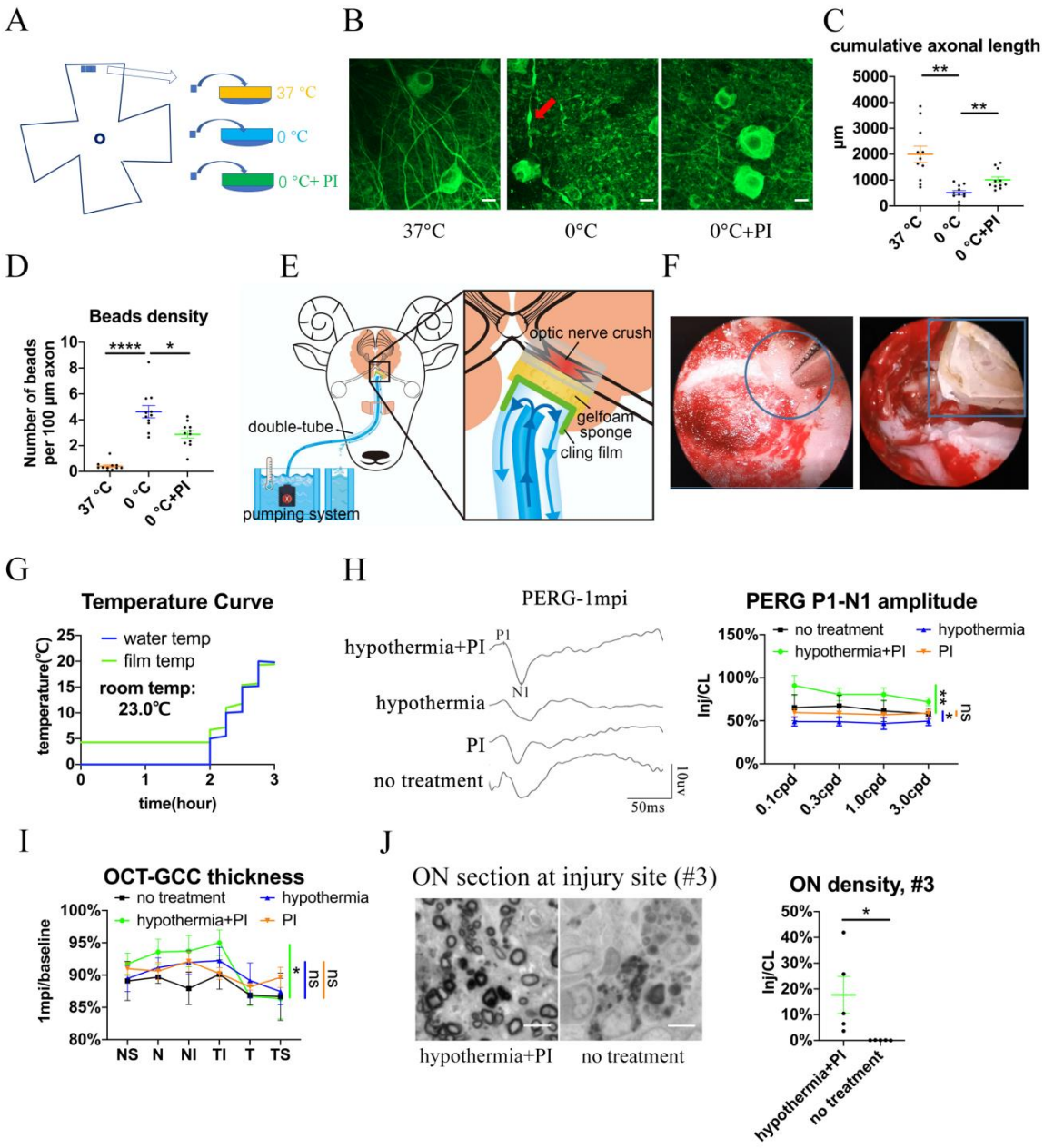

834

835 **Fig. 5. Local delivery of hypothermia combined with cold-protective reagent, but neither**
836 **treatment alone, achieved significant neural protection.** (A)Scheme for the ex vivo
837 experiments shown in (A)- (D). (B) Representative confocal images of retinal explants
838 immunostained with beta-3 tubulin (TUBB3) at 37°C, at 0°C, or at 0°C with PI. A typical
839 axonal bead was labeled by a red arrow. Scale bar: 10 μm. (C, D) Quantification of

cumulative axonal length (C) and axonal beads density (D) at 37°C, at 0°C, and at 0°C with PI. n=11 retinal explants from 4 goats for each group. (E) Scheme of local delivery of hypothermia and protease inhibitors (PI) at the injury site of the pre-chiasmatic ON. (F) Endoscopic image showing placement of a piece of sponge (shown within a circle) (left panel) and a cooling tube (shown within a rectangle) (right panel) at the injured pre-chiasmatic ON. (G) Temperature curves of the cooling water and the cling film during local hypothermia. (H) Representative PERG waveforms at spatial frequency of 0.1 cpd (left panel) and comparison of PERG P1-N1 amplitude ratios at 1 mpi in the following groups: hypothermia combined with PI, hypothermia alone, PI alone, no treatment. n=5-6 in each group. Two-way ANOVA, $p=0.0231$. (I) Comparison of GCC thickness ratio of the injured eyes to the contralateral eyes at six different regions around ON head among each group at 1 mpi. Two-way ANOVA, $p=0.0478$, n=5-6 in each group. (J) Representative images of ON semi-section (left panel) and comparison of axonal densities at the injury site in hypothermia combined with PI, and in a group with no treatment. n=5-6 for each group. Unpaired t-test, $p=0.0398$. Data were presented as mean±s.e.m. ns: not significant, * $p<0.05$, ** $p<0.01$, *** $p<0.001$, **** $p<0.0001$. Inj: injured, CL: contralateral.

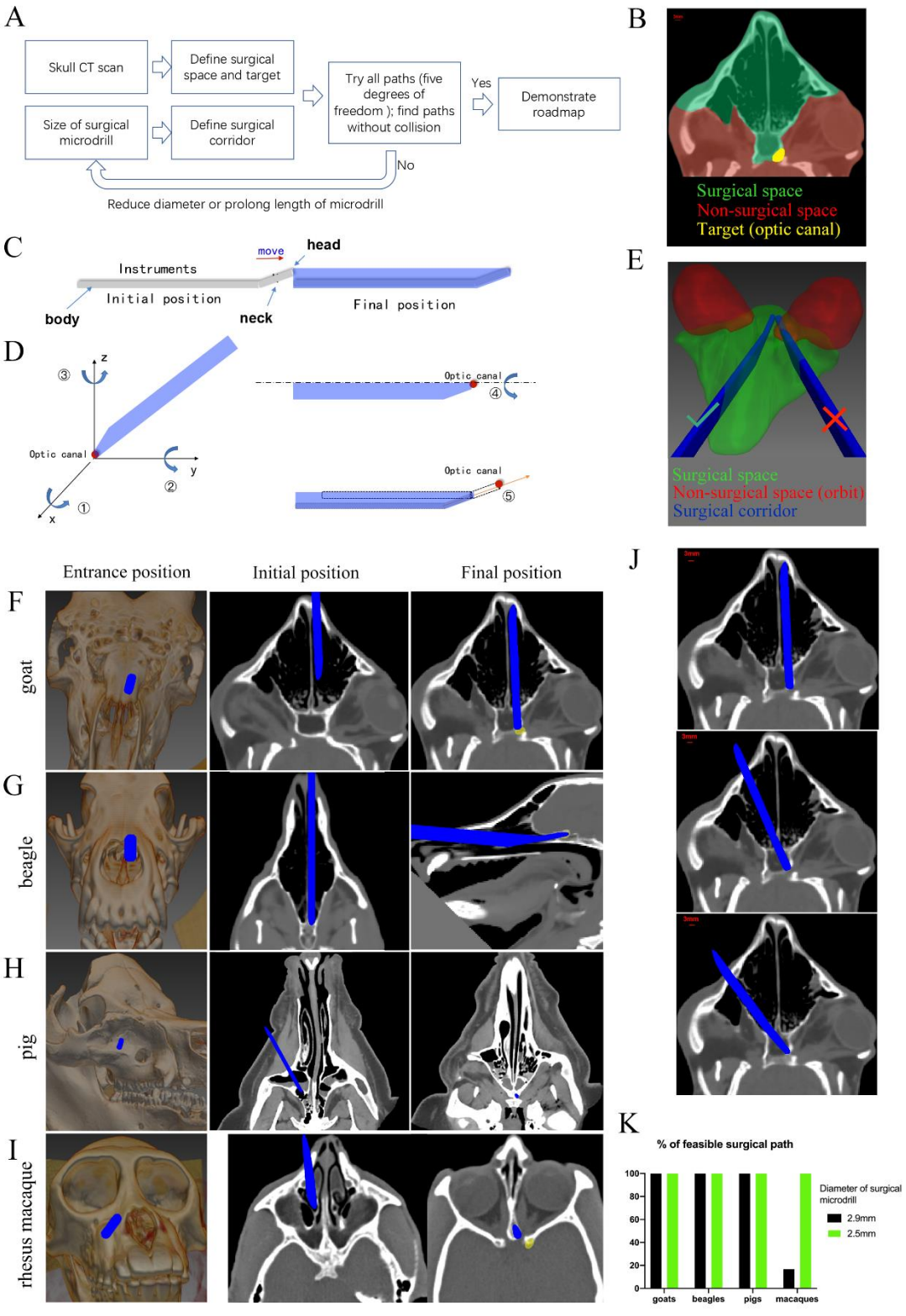

857

858 **Fig. 6. Computer program-aided optimization of trans-nasal endoscopic surgery in**
859 **multiple species of large animals.** (A) Flowchart of the computer program. (B)
860 Segmentation of surgical space (in green), non-surgical space (in red) and surgical target
861 (in yellow) in the program. (C) Scheme of surgical corridor (in blue) outlined by the
862 surgical microdrill's movement along its major axis. (D) Demonstration of five degrees
863 of freedom of the surgical corridor. (E) Demonstration of a feasible surgical corridor (on
864 the left) and an infeasible surgical corridor colliding with orbital cavity (on the right). (F-
865 I) Representatives of virtual surgical paths in goats, beagles, domestic pigs and rhesus
866 macaques, respectively. Surgical entries were shown on the surface of three-dimensional
867 reconstructed skull (left panels) and on the horizontal CT plane (middle panels). Right
868 panels: projection of the surgical corridor on the CT plane through the pre-chiasmatic ON
869 (surgical target). (J) Representatives of multiple feasible virtual surgical paths in goats.
870 Scale bar = 3 mm. (K) Quantification of percentages of feasible surgical paths in goats,
871 beagles, domestic pigs and rhesus macaques by using different sizes of surgical
872 microdrills (diameter = 2.5 and 2.9 mm).
873

Supplementary Materials

894 Movie S8. Representative virtual surgical path to expose the pre-chiasmatic optic nerve in a
895 rhesus macaque.

896 Movie S9. Exposure of the pre-chiasmatic optic nerve via trans-nasal endoscopy in a rhesus
897 macaque.

Supplementary Materials:

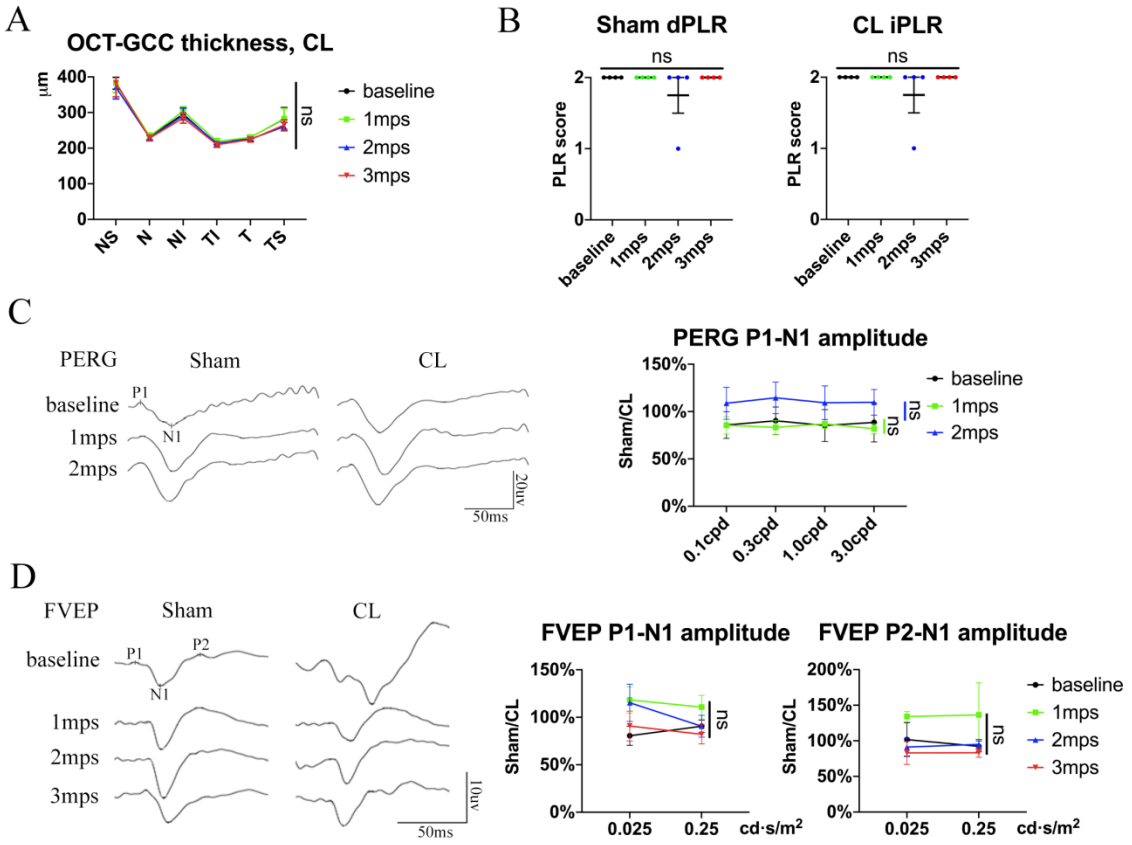

Figure S1. Endoscopic exposure of pre-chiasmatic ON is safe in goats.

(A) Quantification of GCC thickness of the contralateral eyes before and after pre-chiasmatic ON exposure in goats. Two-way ANOVA with Tukey's multiple comparison (compared with baseline). n=4. (B) Quantification of direct pupillary light response (dPLR) in the sham surgical eyes (left panel) and indirect PLR (iPLR) in the contralateral eyes (right panel) after pre-chiasmatic ON exposure. n=4. Friedman test with Dunn's multiple comparison (compared with baseline), p>0.9999. (C) Representative PERG waveforms of the sham surgery eye and the contralateral eye at spatial frequency of 0.1 cpd (left panel) and quantification of P1-N1 amplitude ratios of PERG in the sham surgical eyes to the contralateral eyes (right panel) before

and after pre-chiasmatic ON exposure. n=4. Two-way ANOVA with Sidak's multiple comparison (compared with the baseline). (D) Representative FVEP waveforms of the sham surgical eyes and the contralateral eyes at light intensity of 0.025 cd·s/m^2 (left panel) and quantification of P1-N1 and P2-N1 amplitudes ratios of FVEP in the sham surgical eyes to the contralateral eyes at light intensities of 0.025 and 0.25 cd·s/m^2 (right panel) before and after pre-chiasmatic ON exposure. n=3-4. Two-way ANOVA with Sidak's multiple comparison (compared with the baseline). Data were presented as mean±s.e.m. ns: not significant, CL: contralateral, mps: month post-surgery (post sham surgery).

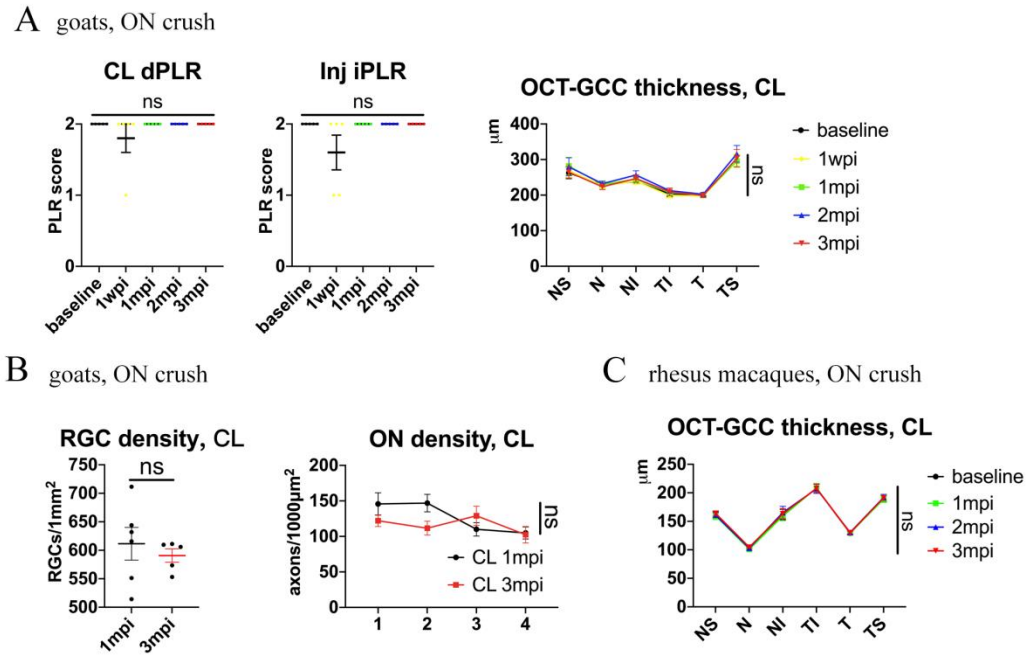

Figure S2. **Contralateral eyes are functionally and structurally intact after ON crush injury.** (A) Left panel: Quantification of dPLR in the contralateral eyes and iPLR in the injured eyes after pre-chiasmatic ON crush in goats. Friedman test with Dunn's multiple comparison (compared with baseline). Right panel: quantification of GCC thickness of the contralateral eyes

after pre-chiasmatic ON crush in goats. Two-way ANOVA with Tukey's multiple comparison (compared with baseline). n=5. (B) Left panel: quantification of RGCs densities of the contralateral eyes at 1, 3 mpi after pre-chiasmatic ON crush in goats. Unpaired t-test. n=5-6. Right panel: quantification of axonal densities of the contralateral eyes at different ON segments at 1, 3 mpi after pre-chiasmatic ON crush in goats. Two-way ANOVA. n=3-6. (C) Quantification of GCC thickness of the contralateral eyes after pre-chiasmatic ON crush in rhesus macaques. Two-way ANOVA with Tukey's multiple comparison (compared with baseline). n=4. Data were presented as mean±s.e.m, ns: not significant, CL: contralateral, wpi: week post-injury, mpi: month post-injury.

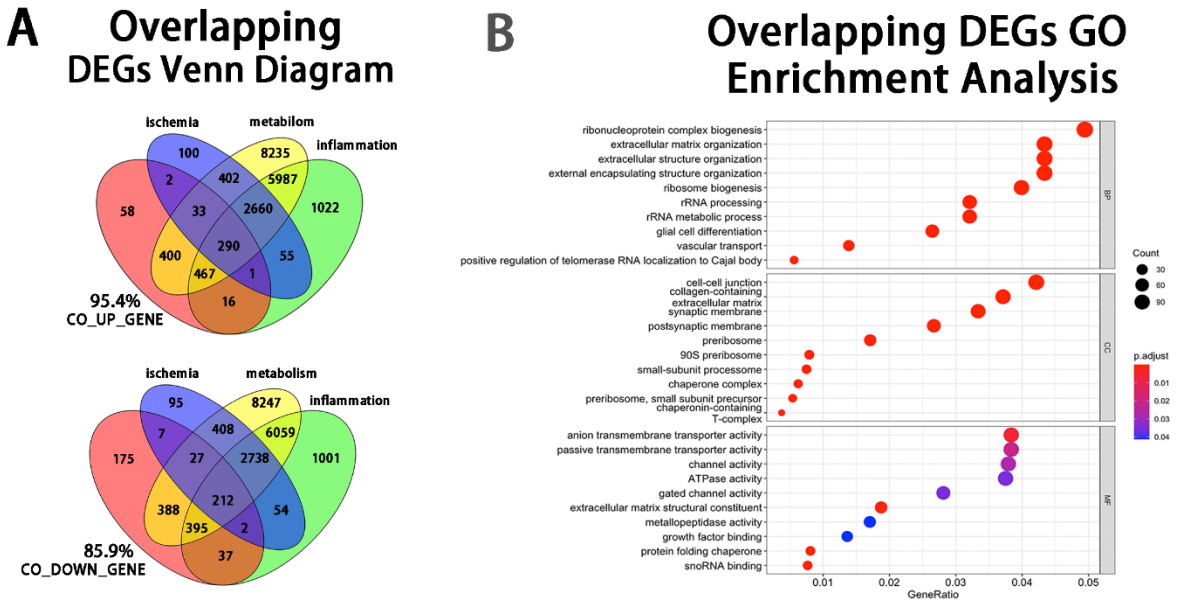

Figure S3. Bioinformatic analyses of the overlapping DEGs at the injury site

(A) Venn diagram showing that 95.4% of the up-regulated and 85.9% of the down-regulated overlapping DEGs at the injury sit were enriched in the pathways of ischemia, inflammation, metabolism.

(B) Enrichment analysis of overlapping DEGs using the Gene Ontology.

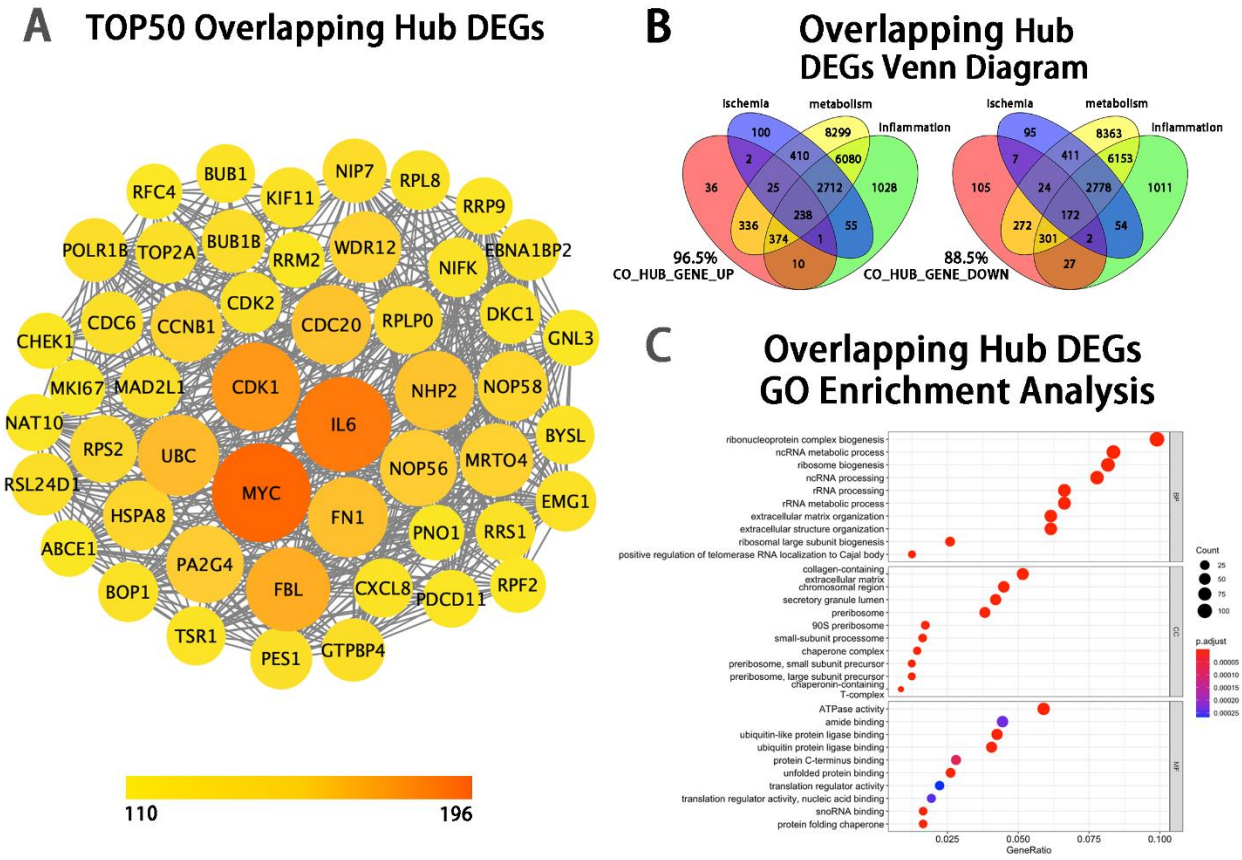

Figure S4. Bioinformatic analyses of the overlapping hub DEGs at the injury site

(A) Protein–protein interactions diagram of top 50 overlapping hub gene (DEGs with highest connectivity). (B) Venn diagram showing that 96.5% of the up-regulated and 88.5% of the down-regulated hub genes were enriched in the pathways of ischemia, inflammation, metabolism. (C) Enrichment analysis of hub genes using the Gene Ontology (GO). (D) Heatmap showing TOP overlapping hub genes enriched in the pathways of ischemia (left panel), inflammation (mid panel) and metabolism (right panel) based on the hub genes of Inj_#3 vs. Ctrl_#3 group. Ranking was determined by the magnitude of fold change.

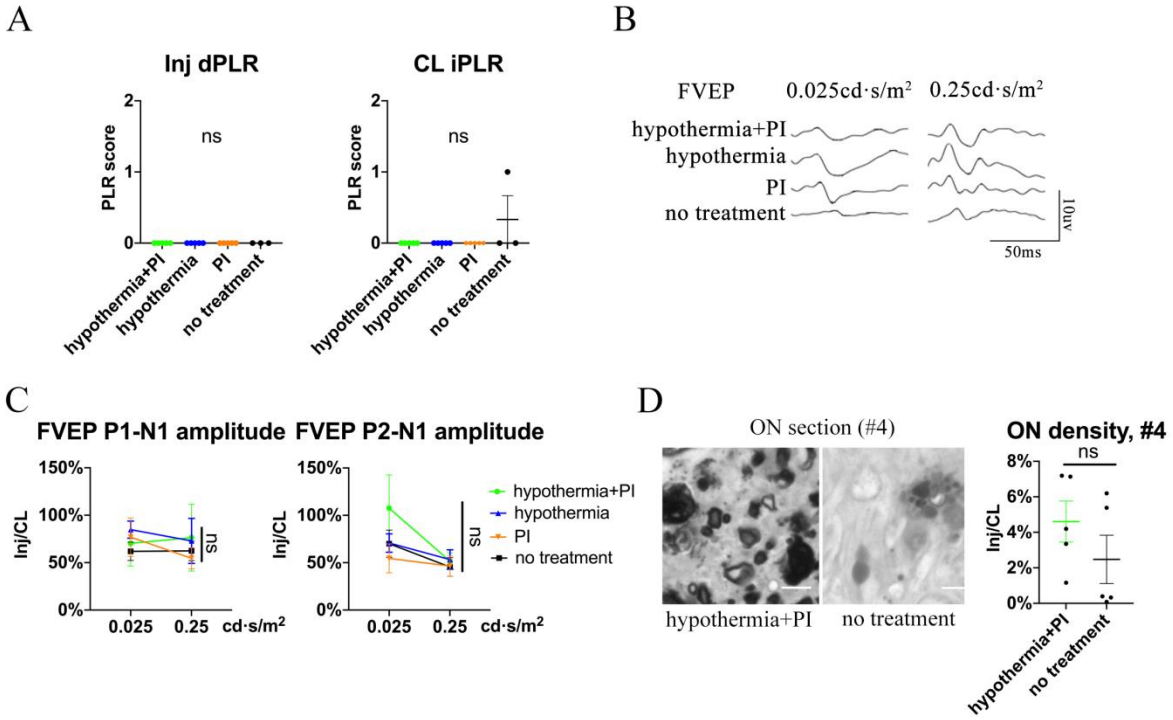

Figure S5. Local hypothermia combined with PI does not show significant rescue of PLR, FVEP, and axonal density at distal ON segment (#4 region)

(A) Quantification of dPLR in the injured eyes (left panel) and iPLR in the contralateral eyes (right panel) in the groups of hypothermia combined with PI, hypothermia alone, PI alone and no treatment. n=5-6 in each group. (B, C) Representative FVEP waveform and quantification of the P1-N1 and P2-N1 amplitudes ratios of FVEP in the injured eyes to the contralateral eyes in each group at 1 mpi. n=5-6 in each group. Two-way ANOVA. (D) Representative images of ON semi-section (left panel) and comparison of axonal densities (right panel) in the groups of hypothermia combined with PI and no treatment at the #4 segment at 1 mpi. n = 5-6 for each group. Unpaired t-test. Data were presented as mean±s.e.m. ns: not significant. Inj: injured, CL: contralateral.

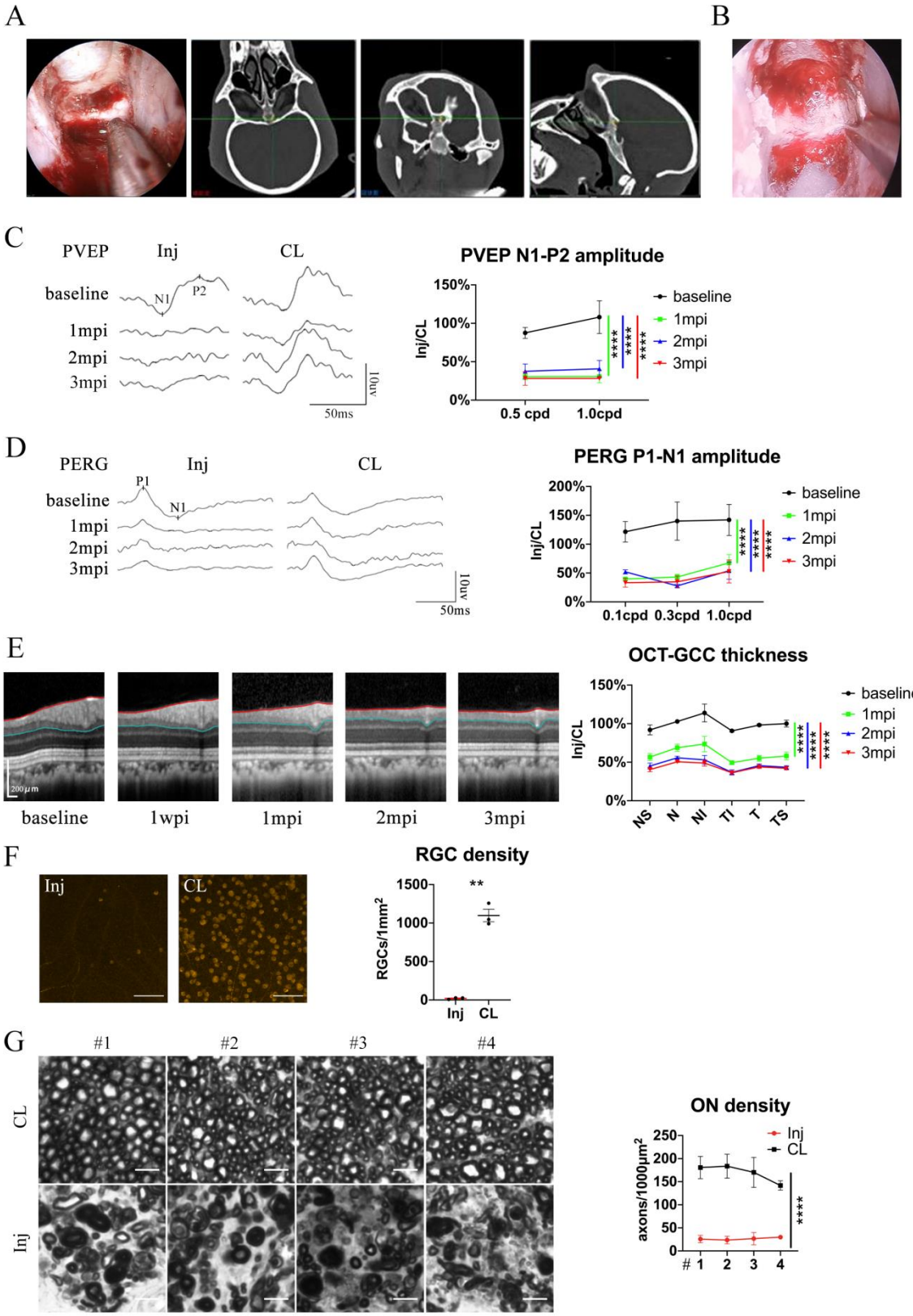

Figure S6. Pre-chiasmatic TON model in rhesus macaque

(A) Confirmation of the pre-chiasmatic ON in rhesus macaques (left panel) using the surgical navigation system on the horizontal, coronal and sagittal CT planes (right panel). (B) Endoscopic image of pre-chiasmatic ON crush. (C) Representative PVEP waveforms of the injured eye and the contralateral eye at spatial frequencies of 0.5 cpd (left panel) and quantification of the N1-P2 amplitude ratios of the injured eyes to the contralateral eyes at spatial frequencies of 0.5 and 1.0 cpd before and after crush (right panel). n=4. Two-way ANOVA with Tukey's multiple comparison (compared with the baseline). (D) Representative PERG waveforms of the injured eye and the contralateral eye at spatial frequency of 0.1 cpd (left panel) and quantification of P1-N1 amplitude ratios of the injured eyes to the contralateral eyes at spatial frequencies of 0.1, 0.3, 1.0 cpd (right panel) before and after crush. n=3-4. Two-way ANOVA with Tukey's multiple comparison (compared with the baseline). (E) Representative OCT images of the injured eye (left panel) and quantification of GCC thickness ratios of the injured eyes to the contralateral eyes at six regions around ON head before and after crush (right panel). n=4. Two-way ANOVA with Tukey's multiple comparison (compared with the baseline). (F) Representative immunostaining images of the RBMPS positive RGCs in the retinal flat-mounts (left panel) and quantification of RGCs densities of the injured eyes and the contralateral eyes at 3 mpi (right panel). n=3. Paired t-test. Scale bar=100μm. (G) Left panel: representative microscopic images of semi-thin cross sections of ON stained by PPD at different ON segments (#1, 2, 3, 4) of the injured eyes and its contralateral eyes at 3 mpi. Scale bar=5μm. Right panel: comparison of axonal densities at different ON sites between the injured eyes and the contralateral eyes at 3 mpi. n=3. Two-way ANOVA. Data were presented as mean±s.e.m. ns: not significant, *:$p<0.05$, **:$p<0.01$, ***:$p<0.001$, ****:$p<0.0001$. Inj: injured, CL: contralateral, mpi: month post-injury.

Movie S1. Surgical settings for trans-nasal endoscopic exposure of the pre-chiasmatic optic nerve in a goat.

Movie S2. Exposure of the pre-chiasmatic optic nerve via trans-nasal endoscopy in a goat.

Movie S3. Crush of the pre-chiasmatic optic nerve via trans-nasal endoscopy in a goat.

Movie S4. Trans-nasal local delivery of hypothermia and protease inhibitors to the injured pre-chiasmatic optic nerve in a goat.

Movie S5. Representative virtual surgical path to expose the pre-chiasmatic optic nerve in a goat.

Movie S6. Representative virtual surgical path to expose the pre-chiasmatic optic nerve in a beagle.

Movie S7. Representative virtual surgical path to expose the pre-chiasmatic optic nerve in a domestic pig.

Movie S8. Representative virtual surgical path to expose the pre-chiasmatic optic nerve in a rhesus macaque.

Movie S9. Exposure of the pre-chiasmatic optic nerve via trans-nasal endoscopy in a rhesus macaque.